



Hernández-Rodríguez, E. W., Escorcia Cabrera, A. M., Van Der Kamp, M. W., Montero-Alejo, A. L., & Caballero, J. (2020). Multi-scale Simulation Reveals that an Amino Acid Substitution Increases Photosensitizing Reaction Inputs in Rhodopsins. *Journal of Computational Chemistry*. <https://doi.org/10.1002/jcc.26392>

Peer reviewed version

Link to published version (if available):  
[10.1002/jcc.26392](https://doi.org/10.1002/jcc.26392)

[Link to publication record in Explore Bristol Research](#)  
PDF-document

This is the author accepted manuscript (AAM). The final published version (version of record) is available online via Wiley at <https://doi.org/10.1002/jcc.26392> . Please refer to any applicable terms of use of the publisher.

## University of Bristol - Explore Bristol Research

### General rights

This document is made available in accordance with publisher policies. Please cite only the published version using the reference above. Full terms of use are available:  
<http://www.bristol.ac.uk/red/research-policy/pure/user-guides/ebr-terms/>

# **Multi-scale Simulation Reveals that an Amino Acid Substitution Increases Photosensitizing Reaction Inputs in Rhodopsins.**

*Erix W. Hernández-Rodríguez<sup>§,\*</sup>, Andrés M. Escorcia<sup>‡</sup>, Marc W. van der Kamp<sup>‡</sup>, Ana L.  
Montero-Alejo<sup>†</sup>, and Julio Caballero<sup>&</sup>.*

<sup>§</sup>Laboratorio de Bioinformática y Química Computacional, Escuela de Química y Farmacia,  
Facultad de Medicina, Universidad Católica del Maule, 3460000 Talca, Chile.

<sup>‡</sup>School of Biochemistry, Biomedical Sciences Building, University of Bristol, University Walk,  
Bristol BS8 1TD, United Kingdom.

<sup>†</sup>Departamento de Física, FCNMM, Universidad Tecnológica Metropolitana, José Pedro  
Alessandri 1242, Ñuñoa, 780-0002, Santiago, Chile.

<sup>&</sup>Departamento de Bioinformática, Centro de Bioinformática, Simulación y Modelado (CBSM),  
Facultad de Ingeniería, Universidad de Talca, Campus Santiago, 1 Poniente No. 1141, Casilla  
721, Talca, Chile.

## **KEYWORDS**

Photosensitization, singlet oxygen, retinitis pigmentosa, implicit ligand sampling, QM/MM  
calculations

## ABSTRACT

Evaluating the availability of molecular oxygen ( $O_2$ ) and energy of excited states in the retinal binding site of rhodopsin is a crucial challenging first step to understand photosensitizing reactions in wild-type (WT) and mutant rhodopsins by absorbing visible light. In the present work, energies of the ground and excited states related to 11-*cis*-retinal and the  $O_2$  accessibility to the  $\beta$ -ionone ring are evaluated inside WT and human M207R mutant rhodopsins. Putative  $O_2$  pathways within rhodopsins are identified by using molecular dynamics simulations, Voronoi-diagram analysis, and implicit ligand sampling while retinal energetic properties are investigated through density functional theory, and quantum mechanical/molecular mechanical methods. Here, the predictions reveal that an amino acid substitution can lead to enough energy and  $O_2$  accessibility in the core hosting retinal of mutant rhodopsins to favor the photosensitized singlet oxygen generation, which can be useful in understanding retinal degeneration mechanisms and in designing blue-lighting-absorbing proteic photosensitizers.

## INTRODUCTION

*Retinitis pigmentosa* (RP) is the most common ophthalmological inherent disease resulting in a (still untreatable) progressive retinal degeneration and eventually blindness<sup>1-3</sup>. Reactive oxygen species (ROS) and electromagnetic radiations can promote retinal degenerations, including RP variants caused by mutations of the gene encoding rhodopsin<sup>4,7</sup>.

Singlet oxygen ( $O_2(a^1\Delta_g)$ , the lowest energy excited electronic state of molecular oxygen) is a very destructive ROS linked to retinal degenerations<sup>8,9</sup>.  $O_2(a^1\Delta_g)$  is frequently generated via the photosensitizing reaction type II<sup>10</sup>, a common photosensitization pathway which demands for molecular oxygen ( $O_2$ ), energy from electromagnetic radiations, and a photosensitizing molecule<sup>10,11</sup>. These requirements are abundant in retina<sup>6,7</sup>, a tissue which houses rhodopsin in photoreceptor rod cells<sup>12,13</sup>.

Studies state an increased retinal susceptibility to light-induced damage for rhodopsin mutants<sup>4,5</sup>. Some authors suggest that even wild-type (WT) rhodopsin exhibits photosensitizing activity associated with retinal degeneration<sup>14-18</sup>. Other studies diminish<sup>19</sup> or discard<sup>9,20,21</sup> rhodopsin as photosensitizer and indicate the free all-*trans* retinal to be the photosensitizing agent responsible for retina damage.

There is also evidence that 11-*cis*-retinal covalently bound to Lys296 in rhodopsin (Figure 1) can act as a photosensitizer and generate  $O_2(a^1\Delta_g)$ . The action spectrum of visible light retinal damage matches that of 11-*cis*-retinal absorption in mammal rhodopsins<sup>17-19,22,23</sup>. The conjugated double bond system of retinal is extended along the region of the chromophore, comprising the  $\beta$ -ionone ring<sup>24</sup>, where the energy transfer<sup>25,26</sup> could occur upon interaction of  $O_2$  with light-excited chromophore. The  $\pi\pi^*$  configuration of retinal can contribute to a more prolonged lifetime of its excited states with respect to those exhibiting  $n\pi^*$ -excited electronic configuration like in other

similar photosensitizing compounds<sup>10</sup>. Besides, the selectivity of the rhodopsin binding pocket (RBP) to covalently bind a unique molecule of retinal<sup>13</sup> can prevent chromophore aggregation phenomena, and consequently non-light-dependent reactions. Intersystem crossing (ISC) between the lowest energy excited singlet state ( $S_1$ ) and the lowest energy excited triplet state ( $T_1$ ) of retinal in protein environments and solutions has also been reported<sup>27-29</sup>. Experimental data show that 11-*cis*-retinal can absorb a photon and react with  $O_2$  in oxygenated solutions to produce  $O_2(a^1\Delta_g)$  efficiently, which is indicative of lifetimes of the retinal  $T_1$ -state sufficient for a photosensitizing reaction type II<sup>28</sup>. Specifically, experimental results show that the  $T_1$  state of the  $\beta$ -ionone moiety acts as a sensitizer generating singlet oxygen<sup>30</sup>. The photosensitized  $O_2(a^1\Delta_g)$  generation can also occur inside proteins by excitation of hydrophobic residues with  $\pi$ -conjugated systems<sup>31</sup>.

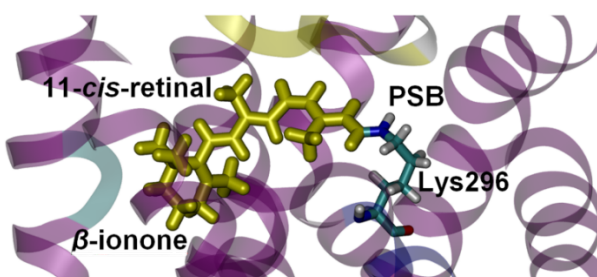


**Figure 1.** 11-*cis*-retinal chromophore covalently linked to Lys296 via a protonated Schiff base in a rhodopsin model built from the crystal structure reported with the PDB code 1U19<sup>32,33</sup>. 11-*cis*-retinal with the  $\beta$ -ionone moiety is shown in yellow licorice. Lys296 is in licorice representation and colored according to atom types.

The photosensitizing role of rhodopsin has been debated for years<sup>9,14-21</sup>. Nevertheless, the accessibility of  $O_2$  to 11-*cis*-retinals at their binding pockets in human WT or mutant rhodopsins is not fully understood, similar to other potential photosensitizers (*e.g.* aromatic residues) in rhodopsins or in other proteins<sup>31</sup>. The access of  $O_2$  to the 11-*cis*-retinal embedded in human WT or mutant rhodopsins can be highly probable due to the diffusion of  $O_2$  in retinal tissue<sup>6,7</sup> and in

bovine rhodopsin among other proteins<sup>25,31,34,35</sup>, the low size and low polarity of this gas molecule<sup>10,11</sup>, non-polar microenvironments across the polypeptidic matrix, including the binding site of the chromophore<sup>13,34</sup>. Marazzi *et al.*<sup>25</sup> reported theoretically a notable accumulation of O<sub>2</sub> to the retinal  $\beta$ -ionone ring in bovine WT rhodopsin. This finding was considered as an indicative for the accessibility of O<sub>2</sub>(a<sup>1</sup> $\Delta_g$ ) to the retinal ring, leading to state an isomerization mechanism based on the generation of excited states through the chromophore oxidation by this reactive oxygen specie. Nevertheless, the chemical reaction described by these authors to propose an additional photoisomerization mechanism, could also induce destructive collateral reactions affecting the structural stability of the  $\beta$ -ionone of 11-*cis*-retinal and of the whole rhodopsin core. The question is whether the O<sub>2</sub> access in the binding pocket of human mutant rhodopsins can be favored as photosensitized O<sub>2</sub>(a<sup>1</sup> $\Delta_g$ ) could also access to this protein core inside bovine WT rhodopsin. To the best of our knowledge, studies at molecular level have not been reported which address any association of the production of O<sub>2</sub>(a<sup>1</sup> $\Delta_g$ ) in rod photoreceptors with molecular changes taking place in mutant rhodopsins embedded in lipidic membrane or in aqueous or non-membrane environments.

Àguila *et al.*<sup>36</sup> demonstrated experimentally that purified M207R mutant absorbs blue light in a non-membrane environment after being genetically expressed and folded as a viable matured rhodopsin in primate cells. Theoretical studies identify and explain the spectral blue shift by modeling human M207R mutant in aqueous environment where the RBP structure was conserved like in membrane<sup>24,37</sup> (Figure 2). Since M207R substitution has been associated with hydrogen bond network perturbation in the retinal binding pocket<sup>37,38</sup>, a loss of protection against the penetration of molecular oxygen in the protein core of this mutant rhodopsin can be expected. Both, the presence of O<sub>2</sub> and the energy excess of the retinal excited state from blue-shifted M207R

mutant, could be requirements sufficiently available for a reaction of photosensitization Type II at the RBP of this stabilized rhodopsin out of membrane under pathological<sup>39,40</sup> or experimental<sup>36</sup> conditions. Interestingly, light-dependent toxicity associated with mutant rhodopsin has been reported in the endoplasmic reticulum and rod outer segment<sup>41</sup>, which suggests a link between genetic causes of RP and the oxidative damage of photoreceptor cells during retinal degenerations<sup>40,42</sup>. The amino acid substitution in the M207R mutant is also interesting for the field of protein engineering since this change induces similar spectral characteristics<sup>36</sup> to those from blue-light-sensitive proteins that are used as optogenetic markers generating  $O_2(a^1\Delta_g)$ <sup>43-45</sup>.

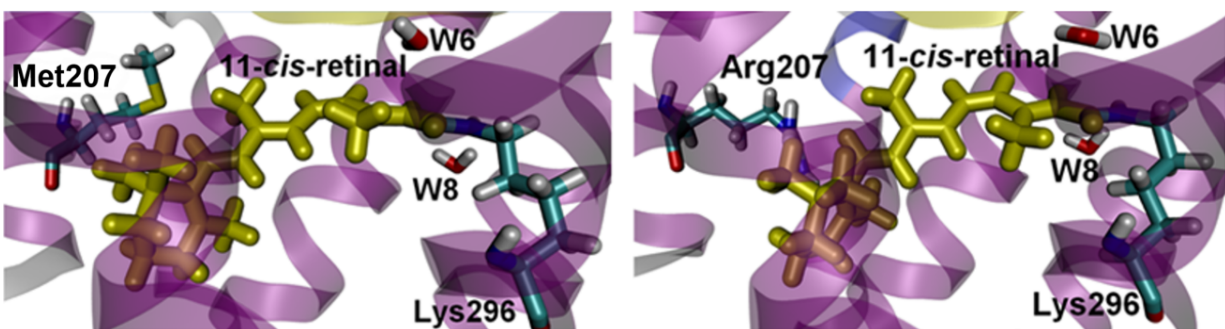


**Figure 2.** Human WT rhodopsin (left) and its M207R variant (right) with 11-*cis*-retinal (yellow licorice) covalently bound to Lys296 via a protonated Schiff base. The mutated residue is located near the  $\beta$ -ionone ring of 11-*cis*-retinal. These structures were obtained by homology modeling as described in the Methods Section. W6 and W8 correspond to water molecules found at the retinal binding site of rhodopsins.

The photosensitized generation of  $O_2(a^1\Delta_g)$  competes favorably with other molecular events *in vivo* and *in vitro* sceneries because it is an ultrafast and diffusion-limited reaction in blue-light-sensitive receptors embedded in biological media<sup>44</sup>. Besides, these are not input limitations (molecular oxygen and light energy) for this type of photosensitizing reaction in the retinal tissue with high exposure to electromagnetic radiation and significant oxygen consumption<sup>46</sup>. Regardless of the normal functioning of the WT rhodopsin like a membrane-integral protein<sup>13</sup>, our principal goal is to study how feasible the photosensitization reaction is in the water-solubilized M207R

mutant rhodopsin. For comparative purposes, and to rationalize the potential of this type of reaction in rhodopsin-like proteins, we use a WT human rhodopsin model under the same conditions. Our study focuses on water-solubilized M207R because there is evidence that this protein folds in non-membrane environment, maintaining its blue-light-sensitive receptor property<sup>36,47</sup>. Moreover, Riedmayr *et al.*<sup>48</sup> recently identified the non-insertion of structural-perturbed M207R mutant rhodopsin in membranes from HEK293 cells and from mouse photoreceptors, showing its localization in the soma and rod inner segments, as well as changes in the mRNA splicing machinery that is regulated by cell type-specific factors. Although the membrane mislocalization of M207R mutant could be due to direct structural effects caused by the mutation, its viable conformation expressed in primate cells<sup>36</sup> could also be mislocalized from membrane because of cellular disorders occurring in retinal degenerations<sup>39,40,42</sup>.

In this work, we apply molecular dynamics (MD) simulations<sup>49</sup> on homology models<sup>50</sup> of human M207R mutant rhodopsin (hM207R) in aqueous solution, simulating one of its possible tissular pathological or *in vitro* environment. Specifically because identifying photosensitizing potentialities, at least for the water-solubilized M207R mutant, allows getting insights into particular retinal degeneration mechanisms<sup>39,40,42</sup> and into protein engineering focused on possible optogenetic marker development<sup>43-45</sup>. MD-equilibrated configurations are used to identify potential transport pathways of O<sub>2</sub> from solvent to the  $\beta$ -ionone ring, using implicit ligand sampling (ILS)<sup>51</sup> and Voronoi diagrams<sup>52</sup>. The former has been widely applied to describe energy-enabled sites and migration paths of O<sub>2</sub> inside different types of proteins<sup>34,51,53-58</sup>, while the latter is useful to compute geometrical properties of O<sub>2</sub>-migration tunnels and their temporal evolutions<sup>52,55,58</sup>. In addition, hybrid quantum-mechanics/molecular-mechanics<sup>59,60</sup> (QM/MM) calculations were performed to compute energies associated with the ground and excited triplet states from QM regions including



the 11-*cis*-retinal chromophore, using density-functional theory (DFT) method<sup>61,62</sup>. Our calculations provide detailed information on the feasibility of photosensitized singlet-oxygen production at the retinal binding pocket of hM207R. This work may open a new avenue in understanding the effects of a single amino acid substitution in RP-linked mutant rhodopsins as well as for applications in the field of photoactive protein engineering regarding production of singlet oxygen.

## METHODS

**Starting structures.** Since the structures of hWT and hM207R rhodopsins are not known experimentally, homology models of their full amino-acid sequence were built according to a protocol similar to that previously reported by authors of this work<sup>37</sup>. Three-dimensional (3D) models were obtained by homology modeling techniques based on the satisfaction of spatial restrictions as implemented in MODELLER 9.11 program<sup>63</sup>. All 3D models of human WT (hWT), and human hM207R mutant (hM207R) rhodopsins were obtained from its homologous bovine rhodopsin (bWT)<sup>64</sup>, using the atomic coordinates of the 2.2 Å resolution crystal structure with PDB code 1U19 (chain B in the dark state conformation)<sup>32,33</sup>.

The homology model of bovine WT rhodopsin (bWT) was also built from its own crystal structure to achieve consistent comparisons. As in our previous work<sup>37</sup>, the rhodopsin sequences were obtained from the TrEMBL and SWISSPROT databases available from the ExPASy Molecular Biology Server<sup>65</sup>, while data to build M207R mutant variants were collected from the literature<sup>36-38</sup>, and from the Human Gene Mutation Database<sup>66</sup>. There is a high similarity between *Bos taurus* and *Homo sapiens* for essential characteristics of the visual pigment associated with the structure, function, cellular topolocalization in the rod photoreceptor, and spectral properties<sup>13,67-69</sup>. This is

further reflected in the high sequence identity between human and bovine rhodopsin (ca. 93 %) <sup>64</sup>, which was also determined by using the Basic Local Alignment Search Tool <sup>70</sup> (BLAST). Moreover, a huge amount of high-quality data has been reported on the high-resolution starting structure (1U19 <sup>32,33</sup>) <sup>13,35,71</sup> used to obtain the structural model of the bovine dark-state in this work. Hence, previous results and those obtained here for the bovine rhodopsin, are appropriate to provide reasonable comparisons during the analysis of the human systems.

Twenty-five models were generated by using the starting structure 1U19 and the corresponding sequence alignments, including within it the position of internal water molecules, which were transferred to homology structures built with all hydrogen atoms. The molecular mechanics (MM) parameters for the protein and retinal linked to protonated and deprotonated Schiff base were taken from the CHARMM force field library <sup>72</sup>. The homology models were energy minimized utilizing the variable target function method (VTFM, normal schedule) and conjugated gradient (CG) algorithm to subsequently be refined by combining MD simulations (normal level) with simulated annealing. The model with the lowest discrete optimized protein energy (DOPE) was selected by applying the DOPE-HR method through the standard MODELLER energy function <sup>63</sup>.

Each resulting model contained the opsin, 11-*cis*-retinal linked to Lys296 via a protonated Schiff base (PSB), a Cys110 – Cys187 disulfide bridge, 29 internal water molecules (as hosted in chain B of bWT <sup>29,30</sup>) with positions as expected according to their coordinates in the crystal structure, and two palmitic acid residues linked to Cys322 and Cys323 <sup>37</sup>. Subsequently, the selected homology models were starting structures for the MD simulations. In addition, a variant of hM207R (hereafter referred to as hM207R<sub>DSB</sub>) was built which involves a deprotonated Lys296 and a neutral Glu113 (residue next to Lys296), with 11-*cis*-retinal being covalently bound to the protein structure via a deprotonated Schiff base (DSB). A DSB in the rhodopsin dark-state

conformation has been hypothesized to be responsible for the spectral blue shift of this mutant in non-membrane environment observed experimentally<sup>36</sup>. Theoretical studies by Hernández *et al.*, however, reproduced a similar behavior of the spectral shift by considering a PSB<sup>37</sup>, due to a reduction of the charge accumulation associated with geometrical distortions at the Schiff-base and central regions of 11-*cis*-retinal<sup>24</sup>.

The protonation states of titratable amino acid residues were assigned according to experimental pH values determined in photoreceptors<sup>73</sup>, visual inspection, and  $pK_a$  calculations by using the PROPKA 3.1 program<sup>74-76</sup> that considers the effect of the 11-*cis*-retinal ligand, as described in our previous work<sup>37</sup>. In bWT and hWT, all titratable residues were charged, except Asp83, Glu122, and Glu181, which is in full agreement with UV-Vis spectra determined in site-directed mutants (for Asp83 and Glu122) and with FTIR experiments performed for bovine-WT rhodopsin<sup>73</sup>. Nevertheless, the protonation state of Glu181 is a controversial issue as ambiguous results have been obtained from other spectroscopic experiments (NMR<sup>77,78</sup>, two photon spectroscopy<sup>79</sup>, crystallization studies<sup>32</sup>, and preresonance Raman vibrational spectra<sup>80</sup>) and from theoretical approximations (MM-MD<sup>81</sup> and QM/MM<sup>80,82</sup> studies). However, the QM/MM calculations have shown the normal absorption-maximum ( $\lambda_{max}$ ) to be very similar for the rhodopsins with a neutral and charged state of this residue<sup>82</sup>. On the other hand, although Glu181 is conserved in the binding pocket of bovine and human rhodopsins, its position is not located close enough to the  $\beta$ -ionone ring of retinal chromophore<sup>13</sup> which could act like a photosensitizer at the RBP.

His195 was protonated at the  $\delta$  nitrogen in the bWT structure. In all rhodopsin models, we assign His65 and His152 to be protonated at the  $\epsilon$  nitrogen, and His100 and His211 were protonated at the  $\delta$  nitrogen only. Thus, the protonation states of these histidine residues are consistent with those assumed from experimental and QM/MM studies<sup>32</sup>. His278 was protonated at the  $\delta$ - and  $\epsilon$ -

nitrogen atoms, which is a residue located at a loop far away from the RBP. A salt bridge established between the negative charge of Glu113 and a protonated Schiff base (protonated Lys296) was also predicted for all models (*i.e.* bWT, hWT, and hM207R) which have been systematically reported for WT rhodopsins from several of the aforementioned experimental and theoretical studies. Asp83 and Glu181 were the only neutral residues predicted in hM207R. Apart from Lys296 and Glu113, the protonation states of other titratable residues were the same for hM207R and hM207R<sub>DSB</sub>. Standard protonation states were assigned for all other titratable residues.

**MD simulations.** All rhodopsins were subjected to MD simulations in explicit water to mimic cytoplasmic non-membrane and *in-vitro* non-membrane conditions, which are possible media for these mature visual pigments<sup>36,48,83-88</sup>. This approach is supported by spectroscopic experiments and combined QM/MM calculations showing that spectral properties of lipid-membrane-solubilized rhodopsin from *Bos taurus* are preserved in non-membrane environments<sup>36,37,68,69,85,86,88-90</sup>. This is in full agreement with the high similarity of the protein conformations in these environments, as observed in the short nanosecond time scale of 11-*cis*-retinal adaptation during MD simulations<sup>37,89,91</sup>. In fact, both in non-membrane and in membrane media, hWT also exhibits an absorption maximum of 493 – 500 nm<sup>92</sup>, while a hypsochromic spectral shift (blue shift) has been described for its mutant hM207R out of membrane<sup>36,37</sup>, being a mislocalized rhodopsin completely absent from membrane in some cell lines<sup>48</sup>.

All rhodopsin structural models were embedded into an octahedral box. The systems with dimensions ca. 95 x 85 x 93 Å contain around 66000 water molecules, keeping 29 internal water molecules transferred from the chain B of bovine rhodopsin, after incorporating them into the alignment during the construction of homology modeling based on the satisfaction of spacial

restrictions. These internal water molecules include the two in the RBP that influence the retinal absorption spectrum of the rhodopsin dark-state conformation<sup>93,94</sup>. All systems were neutralized at near-physiological concentration (200 mM) using Na<sup>+</sup> and Cl<sup>-</sup> ions. The TIP3P model<sup>95</sup> was used for both internal and solvating water molecules. At least 15.0 Å of space was left between the rhodopsin structures and simulation cell boundaries while more than 40 Å of distance was kept between rhodopsin copies of neighboring cells during all MD runs. The palmitoyl residues in the rhodopsin structures were removed, since they are probably only relevant in the membrane environment and in the opsin trafficking when the chromophore is scarce in biological media<sup>13,41</sup>.

All MD trajectories were computed with NAMD 2.7<sup>96</sup> using the CHARMM27 force field<sup>72,97</sup> from which were taken the MM parameters for 11-*cis*-retinal linked to protonated and deprotonated Schiff base. The systems were simulated using periodic boundary conditions (PBC). Long-range interactions for the full systems with PBC were computed using the particle-mesh Ewald method<sup>98</sup> with a grid resolution of < 1.0 Å. All other nonbonded interactions were calculated using a cutoff of 10 Å. SHAKE constraints were applied to all bonds involving hydrogen atoms<sup>99</sup>. A timestep of 2.0 fs was used for all production MD simulations. All systems were simulated at a constant temperature of 300 K and a pressure of 1.0 bar (NPT ensemble) by using the Nosé-Hoover thermostat and barostat<sup>100</sup>.

Before running production simulations, two minimization-equilibration cycles were performed. In the first cycle, all rhodopsin atoms and internal waters were fixed, while the solvating water molecules were relaxed by a 5000-step conjugated gradient (CG) minimization, followed by 100-ps NVT MD simulation. In the second cycle, the protein backbone atoms were fixed and the system was again subjected to 5000-step CG minimization, followed by 100 ps NPT simulation.

Subsequently, a 100 ns (25 ns equilibration; 75 ns production) NPT MD run was performed without applying any positional constraint or restraint.

The MD trajectories and resulting geometries were visualized using VMD 1.9.3<sup>101</sup>. To assess the stability of the systems along the trajectories, we analyzed the time evolution of the root-mean-square deviation (RMSD) for the full protein backbone apart from loops, the rhodopsin binding pocket plus O<sub>2</sub>-gateway regions, and 11-*cis*-retinal. The RMSD profiles show that all rhodopsin structures are stable along the MD trajectories. The significant structural deviations along the trajectories were observed only for loop regions (Figures S1-S3, Supporting Information). The flexible loops do not affect the O<sub>2</sub> gateway regions identified. This conformational preservation of the membrane-integral rhodopsin in water is in agreement with reproducible spectral behaviors determined experimentally for rhodopsins in non-membrane environment<sup>36</sup>, and with results from authors of this work that show the same high conservation of conformational and spectral properties<sup>37</sup>. Specifically for the absorption spectra, protonation states and RBP conformations that were reproduced in good agreement with experiments. In that previous study<sup>37</sup>, the RMSD values ranged from 1.38 to 1.6 Å for WT and mutant rhodopsins, which show a high similarity between RBP of rhodopsin solubilized in water and in lipid POPC membrane.

Since the structures are stable over the timescale of the simulation and the structural reference (PDB code: 1U19<sup>32,33</sup>) corresponds to rhodopsin membrane conformation, it is reasonable to believe that similar conformational sampling would be achieved inside the membrane (perhaps over a longer timescale). A high structural conservation is identified by the superimposition of the protein backbone of the crystalline starting structure 1U19 with those from bovine rhodopsin models calculated in this work (Figure S4, Supporting Information). We consider that the referential water-solubilized model for bovine rhodopsin can also provide more consistent

comparison with experiments. This assumption is based on that investigated properties at RBP of WT and mutant systems (*e.g.* spectral absorption, protonation states) have also been established principally after measuring them for the purified rhodopsins in aqueous and other non-membrane environments<sup>36,79,88</sup>.

For completeness, in addition to the homology models (MD starting structure), we evaluated the structural quality of five equilibrated MD configurations. We used the validation tools VERIFY-3D<sup>97,98</sup>, PROCHECK<sup>99</sup>, and WHAT\_CHECK<sup>100</sup> to evaluate the 3D structure-sequence compatibility (3D/1D profile), the backbone conformations through Ramachandran plot analysis, and the 3D-model fine packing quality, respectively (Table S1, Supporting Information). This evaluation reveals an appropriate internal consistency and the high quality of the 3D models obtained for different steps of the applied methodology.

***QM/MM calculations.*** QM/MM optimizations were performed to calculate the energy gap between the  $T_1$  and  $S_0$  states ( $\Delta E_{T_1-S_0}$ ) and the highest occupied molecular orbital (HOMO) energy related to retinal for the different rhodopsin systems. For this purpose, coordinates of the protein, retinal, and a 26 Å radius water sphere (centred at the C11 atom of retinal) were randomly extracted from MD simulations (Figure 3). Five MD snapshots of each system were selected for QM/MM optimization. Thus, unless mentioned otherwise, all QM/MM energies reported in this study correspond to average values over five snapshots. The QM/MM calculations were performed with the ChemShell package<sup>102-104</sup>, with the Gaussian09<sup>105</sup> and DL\_POLY<sup>106</sup> packages as QM and MM interfaces, respectively. All rhodopsins were optimized using the same QM/MM setup. The QM region consisted of the side chain of Glu113 and the conjugate of Lys296 and 11-*cis*-retinal (Figure 3), and treated at the B3LYP/TZVP level<sup>107-111</sup>. DFT was chosen to describe the QM region, considering the following: i) the use of an extended QM region limits the application of

multiconfigurational methods, ii) the number of systems to calculate for comparative purposes, and iii) the appropriate reproducibility of experimental values associated with energetic properties of retinal that authors of the present work previously reached by using a very similar methodology, QM region, and theory level on the same systems to describe the  $S_1$ -state energy<sup>37</sup>. Although multi-configurational methods should usually be used for such multi-configurational quantum problems, these approaches are limited to a smaller QM region<sup>26,112-114</sup>.

The rest of the system was treated at the MM level using the CHARMM27 force field<sup>72,97</sup>. The total charge of the QM region was zero for all rhodopsins. All atoms within 7 Å of the QM region were unconstrained during optimizations (active region), whereas more distant atoms were kept fixed (Figure 3). All optimizations were carried out using the DL-FIND optimizer module of ChemShell<sup>115</sup>. An electrostatic embedding scheme with charge shift correction was used to compute the electrostatic interaction between the QM region and the surrounding partial charges of the MM region<sup>116,117</sup>. Valencies at the covalent ( $C_\alpha$ - $C_\beta$ ) bonds crossing the QM/MM boundary were saturated using hydrogen link atoms<sup>118</sup>.



Every system was initially optimized with the QM region in  $S_0$  state. Then, the optimized  $S_0$  structure was reoptimized to calculate the  $T_1$  state using the unrestricted Kohn-Sham self-consistent field approximation. The retinal-related ionization potential ( $IP_{approx.}$ ) was approximated as the negative of the HOMO energy of the QM region in the ground state, according to Koopmans' theorem<sup>119</sup>. The chosen QM/MM setup is similar to previous studies reported in the literature<sup>120-123</sup>. Briefly, we used ChemShell with the MM parameters from our MM MD studies and link atoms placed on the  $C_\alpha$ - $C_\beta$  bonds of Glu113 and Lys296 to select the aforementioned QM region as described in Figure 3.

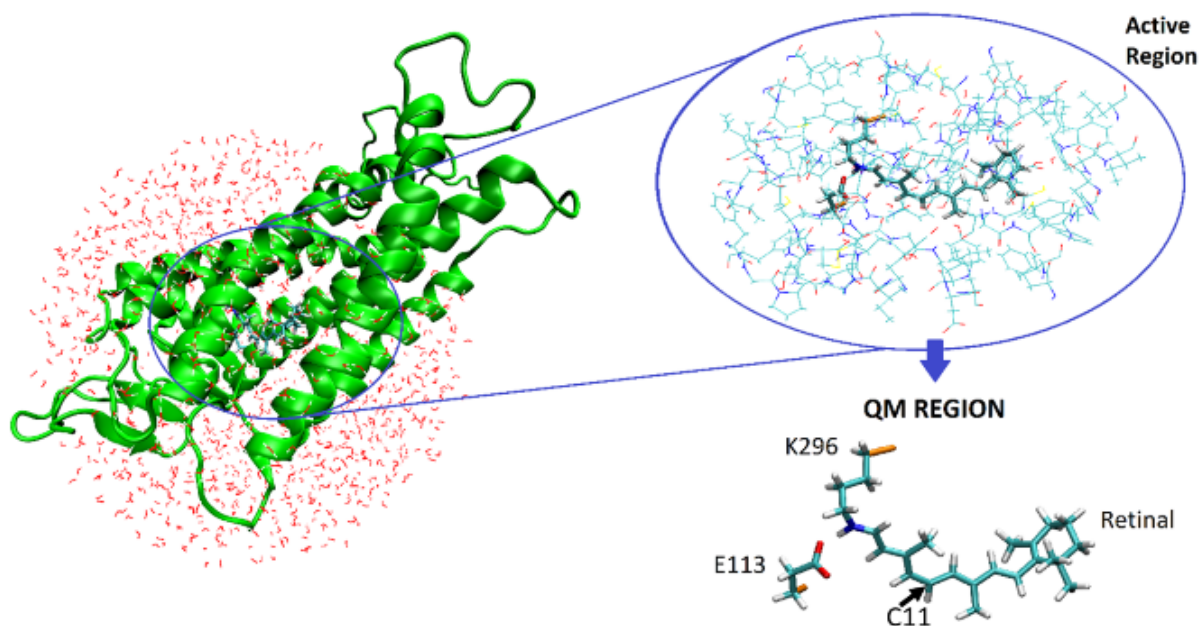


**Figure 3.** Schematic view of the setup used for QM/MM optimization of all rhodopsins - bWT is shown as example. Both Glu113 and Lys296 were charged in bWT, hWT, and hM207R, while uncharged in hM207R<sub>DSB</sub>. QM/MM boundary atoms are shown in orange (QM region, bottom right). It is also highlighted the centre (C11 atom of retinal) of the 26 Å radius water sphere.

**Implicit ligand sampling (ILS) calculations.** The ILS method<sup>51</sup> was applied to each system using five thousands rhodopsin conformations evenly distributed in the final 75 ns of the MD trajectories for all systems. On the other hand, it is important to mention that the amount of MD frames (5000)

used to compute the O<sub>2</sub>-PMF values prevents overestimation errors that could otherwise originate due to insufficient sampling of favorable rare events, as is proved by previous studies<sup>51,53</sup>. Specifically, the ILS method allows to assess sites and migration pathways of O<sub>2</sub> within simple and conjugated proteins, by computing the variation of the free energy ( $\Delta G$ ) associated with transferring an oxygen molecule from vacuum to a particular position into the polypeptide matrix<sup>51</sup>. The ILS calculations were then used to generate 3D  $\Delta G$  maps of placing an oxygen molecule inside the WT and mutant rhodopsins, which allowed us to evaluate the O<sub>2</sub> accessibility near each component of the whole structure of these visual pigments. This identified the access sites of O<sub>2</sub> for the whole protein structure and for the retinal chromophore at the RBP, by means of the calculated O<sub>2</sub>-PMF 3D maps.

The ILS free energy cost of transferring O<sub>2</sub> into the rhodopsin structure ( $\Delta G_{O_2-RHO}$ ) was computed for each simulation frame divided into a regularly-spaced grid of 1.0 Å in all three dimensions (1.0 Å<sup>3</sup> voxels). For O<sub>2</sub>, 40-randomly rotational orientations per voxel were evaluated in each position on a 3 x 3 x 3 Å subgrid. The van der Waals (vdW) parameters for O<sub>2</sub> were an  $\epsilon_O$  of -0.12 kcal/mol and a vdW radius ( $R_{\min,O}/2$ ) of 1.70 Å, as is described in CHARMM27 and CHARMM36 force fields. All calculations were performed at the same constant temperature of 300 K used in MD simulations.

We used a free energy profile (FEP) based on the ILS calculations to determine energetic properties of O<sub>2</sub> migration pathways from outside the rhodopsin structure to the  $\beta$ -ionone ring. Specifically because the calculated O<sub>2</sub>-PMF isosurfaces identified that the  $\beta$ -ionone moiety was the most accessible component to molecular oxygen inside all rhodopsin structures, with the rest of the RBP much less accessible to this gas molecule. In fact, the average O<sub>2</sub> PMF values represented by these iso-energy surfaces showed a clearly low probability of finding O<sub>2</sub> pathways

that end at other chromophore regions. Therefore, we focused on O<sub>2</sub> pathways toward the  $\beta$ -ionone ring of retinal, which was also advantageous for homogeneity in the comparisons. The FEP was calculated by plotting  $\Delta G_{O_2-RHO}$  values as a function of the distance between two points: (i) the starting point, which is located in a bulk solvent region near an access point to the cavity of the protein, and (ii) the ending point, which corresponds to the mass center of the  $\beta$ -ionone ring. Since the end point represents punctual coordinates attributable to a molecule moiety instead of representing the complete molecule size, it was necessary to consider a collision sphere (*i.e.* spherical region where the O<sub>2</sub>-ring interaction is probable considering interatomic distances). The latter was of 3.0 Å radius, with origin in the ring mass center.

The radius of the collision sphere matches with the starting distance used to search geometrical tunnels from the retinal ring in the rhodopsin systems (*vide infra*) and was assigned the value of the CHARMM force-field vdW radius parameter for O<sub>2</sub> ( $R_{\min,O}/2 = 1.70$  Å). The  $\Delta G_{O_2-RHO}$  calculations corresponding to each FEP were based on an *ad-hoc* TCL program that can be found elsewhere<sup>124</sup>. The FEP calculations were also guided by previous representation of the Voronoi diagram and O<sub>2</sub> potential-mean-force (PMF) maps (Figures 6, 7, Figure S5 in Supporting Information). A very low variation of the measured O<sub>2</sub>-PMF values was identified at several regions of the bulk solvent, as reflected by a low usual sampling error of 0.45 kT every 2 ps. We calculated the  $\Delta G_{O_2-RHO}$  value into a box containing the  $\beta$ -ionone ring at the RBP from the minimum and maximum coordinates of this retinal moiety. The free energy of placing dioxygen into the nearest vicinity of the cyclohexenyl part of the chromophore is hereafter called  $\Delta G_{O_2-ring}$ . The calculation of the solvation energy of O<sub>2</sub> in water ( $\Delta G_{O_2-solv}$ ) was performed on the average PMF values obtained from a box that contains bulk solvent water molecules, using 5000 simulation frames from the equilibrated dynamic trajectory. The  $\Delta G_{O_2-solv}$  values corresponded to a random

position in the bulk water, considering the solvent homogeneity between systems. For validation purposes, the computed  $\Delta G_{O_2-solv}$  value was compared to the reported experimental one. The regions that may host molecular oxygen inside the rhodopsin structures were identified from O<sub>2</sub>-PMF 3D maps, by representing isoenergy surfaces at the contour values of  $-1.0$  and  $1.0$  kT. The VMD program was used to perform the ILS analysis and to visualize the results.

**Voronoi-diagram calculations.** The Voronoi-diagram (VD) method was performed on the same conformational space (the same 5000 simulation frames) used in the ILS analysis. The methodology allowed us to compute and to visualize geometrical properties of potential tunnels of dioxygen in the rhodopsin conformations, using the CAVER<sup>52,125</sup> program (version 3.02) and the CAVER Analyst<sup>126</sup> tool (version 2.0). By subsequently placing spheres on a grid from the protein interior to the outside environment by means of VD calculations, the CAVER program builds tunnels connecting the buried sites of the polypeptide matrixes to the solvent bulk. This methodology allowed us then to characterize geometrically all possible O<sub>2</sub>-migration pathways ending near ( $3.0 \text{ \AA}$ ) the mass center of the  $\beta$ -ionone ring. The geometrical similarity between pathways from different simulation frames was analyzed by clustering techniques, as implemented in the CAVER 3.02 program. The O<sub>2</sub> tunnels were evaluated according to the parameters: throughput, length and bottleneck radius. The tunnel search with the CAVER algorithm was started at  $3.0 \text{ \AA}$  from the mass center of  $\beta$ -ionone ring, in agreement with the collision sphere radius used in the ILS analysis. The minimum probe radius was of  $0.9 \text{ \AA}$ , which has been used to identify O<sub>2</sub> tunnels in a previous study<sup>58</sup>. The shell radius and shell depth were set to  $5.0$  and  $4.0 \text{ \AA}$ , respectively. Default values were applied to the remaining parameters. All data were visualized with the VMD program to facilitate an integrated analysis with the ILS results.

## RESULTS AND DISCUSSION

**Evaluation of the availability of O<sub>2</sub> near the 11-*cis*-retinal  $\beta$ -ionone ring of the rhodopsins embedded in water solution.** As mentioned above, since the O<sub>2</sub>-PMF isosurfaces allowed to identify that the  $\beta$ -ionone moiety was the retinal part accessed systematically by molecular oxygen, while other regions of the chromophore were not sufficiently connected to transport this gas molecule, we emphasized our analysis on the O<sub>2</sub> migration toward the chromophore ring. The prediction of O<sub>2</sub> pathways is based on the steric and energetic viability for the migration of the gas molecule from the solvent to inside the rhodopsin structures: the O<sub>2</sub> pathways have to be favorable from both geometric and energetic standpoint. These two factors are first addressed separately below.

*Steric viability of O<sub>2</sub> migration pathways toward the  $\beta$ -ionone ring.* Steric viability was assessed by calculating possible tunnels from using the CAVER program<sup>52,125</sup> as well as by implicit ligand sampling (ILS) calculations<sup>51</sup> (to consider energy-enabled pathways). Both were performed on five thousand rhodopsin conformations sampled from the final 75 ns of 100 ns MD trajectories for all systems. In the following, the denotation of <sub>E</sub>, <sub>GC</sub>, and <sub>G</sub> letters is used to represent the energetic routes, geometrical tunnels clusters, and the geometrical tunnels with the highest throughput values (geometrical top tunnels), respectively.

The most favorable geometrical tunnels (A<sub>G</sub> and B<sub>G</sub>) and the lowest-energy routes (A<sub>E</sub> and B<sub>E</sub>) coincide in bWT rhodopsin, identifying two pathways (A and B) for the passage of O<sub>2</sub> through the space available between helices H5 and H6 (Figures 4 and S6 in Supporting Information).

The steric and energetic permissibility of pathways A and B are further supported by the high spatial matching of the energy-enabled routes (A<sub>E</sub> and B<sub>E</sub>) with all calculated geometrical tunnels of the top clusters A<sub>GC</sub> and B<sub>GC</sub> (including the A<sub>G</sub> and B<sub>G</sub> channels; Figure S7 in Supporting

Information). The results also show that O<sub>2</sub> can access the  $\beta$ -ionone ring in bWT but the rest of the protein is much less accessible. This finding is consistent with a spectroscopy study on bWT, where rhodopsin conformational changes have been monitored by recording the collision rates of O<sub>2</sub> with a labeled retinal analogue carrying a nitroxide tetramethyl-oxypyrrolidine instead of the  $\beta$ -ionone ring<sup>35</sup>. This study indicates a certain level of O<sub>2</sub> accessibility to the RBP. Besides, our predictions are in full agreement with recent theoretical results that show a predominant access of O<sub>2</sub> to the retinal ring of the bovine rhodopsin embedded in lipidic membrane<sup>25</sup>.

This congruence, and the high conformational conservation, between rhodopsins in membrane and in non-membrane environments, lead us to consider that our comparative approach could also be coherent to understand the most general features of possible photosensitizing events associated with membrane-solubilized WT rhodopsins.

Recently, dimers of bovine rhodopsin have been identified *in vivo* by a study that also confirms the native single isoform of mature rhodopsin in rod photoreceptors. The primary dimer interface is established by helices H1 and H8 (H1/H8 interface)<sup>87</sup>, without implicating helices H5- H7. Thus, the predicted access of O<sub>2</sub> to the retinal ring in bWT and human rhodopsins through the H5 – H6 and H6 – H7 gates (see Figures 4 and S6) is still available in the dimeric state.

We identified a significant protection level against the penetration of O<sub>2</sub> at the RBP of hWT rhodopsin. In contrast to bWT, spatial correspondences were not found between the geometrical tunnel C<sub>G</sub> and the lowest-energy path C<sub>E</sub> identified at the H5 – H6 gate of the hWT rhodopsin (Figure 4). The tunnel C<sub>G</sub> shows a steric permissibility for a probe of radius 0.9 Å to travel to the

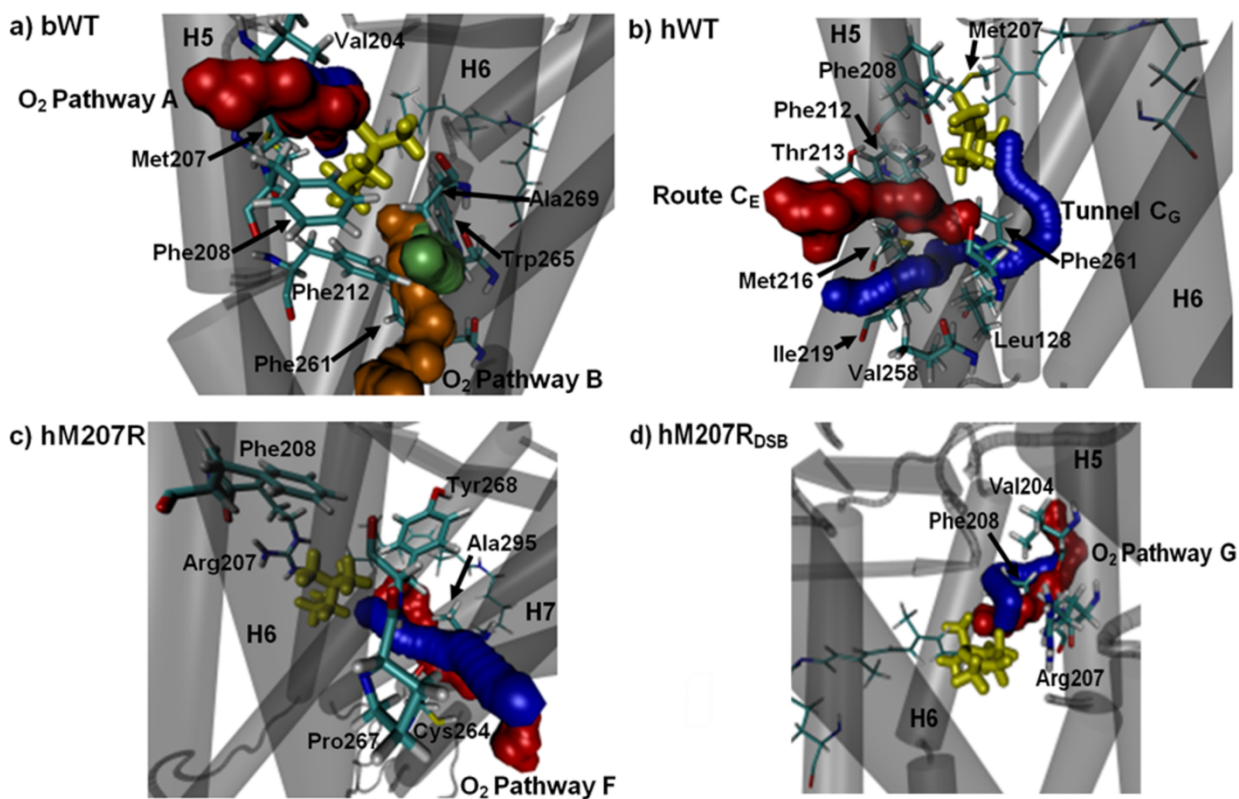


**Figure 4.** Pathways of O<sub>2</sub> migration from the aqueous solvent to the  $\beta$ -ionone ring (yellow licorice) in bWT (pathways A and B at the H5 – H6 gate), hM207R (pathway F at the H6 – H7 gate) and hM207R<sub>DSB</sub> (pathway G at the H5 – H6 gate) rhodopsins. The respective geometrical tunnels (in blue or green) and energy-enabled routes (in red or orange) are shown in solid surface representation. Bottleneck residues are also shown around the geometrical top tunnels (blue/green) and lowest-energy routes (red/orange) identified for the migration of O<sub>2</sub> toward the  $\beta$ -ionone ring (yellow licorice) for all rhodopsin systems. Protein structures are represented in gray cartoon with helix labels.

$\beta$ -ionone ring (Table 1; Figures 4, S6 and S7). In addition, C<sub>E</sub> corresponds to an unfavorable energetic path ending far away from the retinal ring (Figure 4). Two non-top-five additional sets in the clustering-analysis ranking of tunnels (clusters D<sub>GC</sub> and E<sub>GC</sub>) were analyzed for comparison to the mutant systems. Tunnels from the D<sub>GC</sub> and E<sub>GC</sub> clusters have similar spatial distributions to

the top channels found in the mutant systems, however, the tunnel coordinates from these clusters do not match with any energetically feasible route of O<sub>2</sub> in the hWT model (Figure S8 in Supporting Information).

Contrary to the hWT rhodopsin, two O<sub>2</sub> pathways, F and G, were identified for both variants of the mutant rhodopsin. Pathway F, found in hM207R rhodopsin, crosses a cleft between the H6 and H7 helices along the trajectory toward the retinal ring. Pathway G, found in hM207R<sub>DSB</sub>, enters the protein at the H5 – H6 gate, similar to the channel A<sub>G</sub> in the bWT model (Figure 4). Clustering analysis reveals that the tunnel clusters F<sub>GC</sub> and G<sub>GC</sub>, including the top channels F<sub>G</sub> and G<sub>G</sub>, match spatially with the O<sub>2</sub> pathways predicted by ILS calculations (Figure S7).

Interestingly, these O<sub>2</sub> pathways cross the hM207R and hM207R<sub>DSB</sub> structures at different sites (Figure 4), which suggests significant conformational variations between the mutant systems. Since the difference between the models of these mutants is the protonation state assigned to the Glu113 residue and Schiff base, the rupture of the OE2<sub>Glu113</sub> – NZ<sub>Lys296</sub> interaction is responsible of these conformational differences identified for hM207R and hM207R<sub>DSB</sub> (Table S2, Supporting Information). It has been proved that the OE2<sub>Glu113</sub> – NZ<sub>Lys296</sub> salt bridge stabilizes the rhodopsin dark-state conformation and consequently a deprotonated Schiff base leads to lose this electrostatic interaction (*e.g.* in metarhodopsin II) and to conformational interconversions<sup>13</sup>. In addition, the stabilizing hydrogen bond network of the RBP is highly perturbed in both M207R mutants compared with hWT (Table S2, Supporting Information). Therefore, it can be expected that hM207R and hM207R<sub>DSB</sub> behave like two different conformational variants depending on the OE2<sub>Glu113</sub> – NZ<sub>Lys296</sub> salt-bridge formation. Consistent with this, the backbone RMSD value calculated between conformations from the last MD frame for each mutant is ~3.7 Å. Similarly, the backbone RMSD values are ~4.2 and ~5.1 Å for hWT-hM207R and hWT-hM207R<sub>DSB</sub>



comparisons, respectively (Figure S9 in Supporting Information). Therefore, different patterns for the corresponding geometric (tunnel  $F_G$  or  $G_G$ ) and energetic (route  $F_E$  or  $G_E$ ) component of the pathway (F or G) can also take place between structures of these WT and mutant variants of human rhodopsins (Figures 4 and S5-S7).

The geometrical characterization of potential  $O_2$  tunnels shows in detail parameters of the steric permissibility for  $O_2$  to migrate to the retinal ring in the analyzed rhodopsins. For bWT, the bottleneck radii of the geometrical tunnels  $A_G$  and  $B_G$  were larger than the probe-radius value of 0.9 Å. The channel  $B_G$  was the most favorable geometrically, according to the throughput parameter that reflects the compromise between the diameter and length of each tunnel. However, the largest bottleneck radius of 1.14 Å for the tunnel  $A_G$  indicates lower steric hindrance at the narrowest tunnel sector. While the tunnel  $C_G$  is geometrically viable for a probe and bottleneck radius of 0.9 Å in the hWT structure, the throughput value of this channel is the lowest calculated (0.168) due to the smallest width and largest length measured among all systems (Table 1). In hWT, tunnel  $C_G$  is identified as the highest-hindrance path for  $O_2$  to reach the retinal ring, which is consistent with the low population of tunnels found by cluster analysis and the energetic unfeasibility for the tunnel  $C_G$  (Table 1; Figures 4 and S7). In comparison to the tunnels in bWT, a large number of bottleneck residues are directly associated with the narrowness of the channel  $C_G$  in the hWT structure.

The bottleneck radius and throughput values of the channels  $F_G$  (hM207R) and  $G_G$  (hM207R<sub>DSB</sub>) are larger than those calculated for hWT, indicating shorter length and larger width for the geometrical channels for  $O_2$  migration in both mutants. In fact, the steric viability of the channels  $F_G$  and  $G_G$  is similar to those from the bovine system in terms of throughput values.

**Table 1. Geometrical characterization of tunnels for O<sub>2</sub> migration from the aqueous solvent to the  $\beta$ -ionone ring of retinal in bWT, hWT, hM207R and hM207R<sub>DSB</sub> rhodopsins.**

Geometrical Property	Tunnel A <sub>G</sub> (bWT)	Tunnel B <sub>G</sub> (bWT)	Tunnel C <sub>G</sub> (hWT)	Tunnel D <sub>G</sub> * (hWT)	Tunnel E <sub>G</sub> * (hWT)	Tunnel F <sub>G</sub> (hM207R)	Tunnel G <sub>G</sub> (hM207R <sub>DSB</sub> )
<b>Bottleneck radius</b>	1.14	1.02	0.9	0.98	1.04	1.12	1.05
<b>Length</b>	14.95	8.25	25.17	15.61	13.92	10.25	13.67
<b>Throughput</b>	0.52	0.64	0.17	0.45	0.47	0.56	0.63

The bottleneck radius and length are given in Angstroms (Å). \*The energetically unfeasible channels D<sub>G</sub> and E<sub>G</sub> are geometrical top tunnels from the clusters E<sub>GC</sub> and D<sub>GC</sub> (see Figure S8 in Supporting Information), and are spatially comparable with the pathways F and G in hM207R and hM207R<sub>DSB</sub>, respectively.

Therefore, these values indicate less steric hindrance for the O<sub>2</sub> migration through the tunnel of each mutant with respect to the energetically unfeasible tunnels D<sub>G</sub> (top from D<sub>GC</sub> cluster) and E<sub>G</sub> (top from E<sub>GC</sub> cluster) in the hWT model (Table 1; Figure S8). Thus, it is expected that the difference in conformational sampling in both mutants lead to changes in the relative positions of amino acids that facilitate the penetration of dioxygen toward the  $\beta$ -ionone moiety through the interhelix gates.

Variations in the geometrical features between systems are implicated in the critical limiting bottlenecks for passage of O<sub>2</sub> through the tunnels. The side chains of the bottleneck residues Val204 and Phe208 on helix H5 of bWT rhodopsin line a narrow passageway through the tunnel A<sub>G</sub> for O<sub>2</sub> coming from the aqueous environment. The channel A<sub>G</sub> is present while Met207 and Phe208 do not interact. Both gatekeeper residues (Val204 and Phe208) are identified within 3.0 Å of the bottleneck of the tunnel A (Figure 4). In the case of the route B<sub>G</sub>, Phe212, Phe261, Trp265 and Ala269 are identified at the same contact distance for the bottleneck with conformations oriented to the O<sub>2</sub> path (Figure 4). Phe212 on the helix H5 is a gatekeeper interacting with Ala269 positioned on the H6 helix.

The other bottleneck residues of the channel  $B_G$  are both placed on helix H6 of bWT rhodopsin. Both Ile213 and Leu216 also contribute to the hydrophobicity of these  $O_2$  passages, according to previous results that identify to the former as one of the amino acid residues at the entrance to the bovine rhodopsin structure for this gas molecule<sup>25</sup>. Thus, the migration of  $O_2$  through the groups lining the H5 – H6 gate is consistent with the propensity of apolar residues to form  $O_2$  pathways<sup>34</sup>. In the hWT model, seven residues are detected within 3.0 Å of the  $C_G$ -tunnel bottleneck: Leu125, Leu128, Phe212, Met216, Ile219, Ala258 and Phe261. The side chains of Leu125 and Leu128 are oriented from helix H3 to those of Ala258 and Phe261 positioned on helix H6, and the side chains of Met216 and Ile219 are projected to the H5 – H6 gate. In bWT, the amino acid residues isoleucine and leucine occupy the positions 213 and 216, respectively, whereas threonine and methionine are present at these positions in the hWT structure (Figure 4). Thus, the decrease in hydrophobicity at the H5 – H6 gate for hWT could explain preventing  $O_2$  migration through this passageway, with respect to bWT. The sequence identity between bWT and hWT is ~93 and 100 % for the whole protein structure and for the RBP, respectively<sup>37,64,127</sup>. However, the migration of  $O_2$  could be influenced not only by the changes at the positions 213 and 216<sup>34,51</sup> at the H5 – H6 gate but also by the interactions observed between Met207 and Phe208 in the hWT simulations.

The Val204 – Phe208 cleft is crossed by the channel  $B_G$  in the bWT system, whereas the side chain of Phe208 in the hWT model is closer to Val204 due to the orientation of Met207 to interact favorably with the former at a distance lower than 5.0 Å (Figure 4). Since the methionine-aromatic motif are known stabilizing interactions in proteins that can occur in the range 3.4 – 4.8 Å<sup>128</sup>, the Met207– Phe208 interaction can be a significant factor that affects the  $O_2$  migration throughout the Val204 – Phe208 cleft at the H5 – H6 gate in hWT rhodopsin.

In the tunnel  $F_G$  at the H6 – H7 gate in the hM207R system, residues Ala295, Pro267, Cys264, and Tyr268 are in the contact distance of 3.0 Å of the bottleneck, with the first two acting as hydrophobic gatekeepers lining the entrance. Except for Ala295, the remaining bottleneck residues are placed on helix H6 (Figure 4). The M207R substitution leads to a loss of the hindering effect of the Met207 – Phe208 interaction for passage of dioxygen at H5 – H6 gate. The gas molecule can sterically access the collision region near the  $\beta$ -ionone ring at the RBP through the tunnel  $G_G$  that crosses the hydrophobic microenvironment defined by Ala204 and Phe208 at the H5 – H6 gate (Figure 4).

A better understanding on the steric viability for dioxygen transport along VD tunnels comes from the analysis of the radius as a function of the  $O_2$ -passaway length. In the bovine rhodopsin, the radii of the tunnels  $A_G$  and  $B_G$  can reach values higher than 1.2 Å corresponding to the size of a water molecule in the CAVER formalism<sup>55</sup>, especially into the vicinity of the  $\beta$ -ionone ring (Figure 5).


The  $C_G$ -tunnel radius is near to the minimum width around 3.0 Å from the  $\beta$ -ionone moiety inside the hWT rhodopsin (Figure 5). Thus, the permeability of the tunnel  $C_G$  is significantly reduced in the proximity of the retinal ring into the RBP with respect to the tunnels of the bWT model. In the mutant M207R variants, the radius of each tunnel,  $F_G$  or  $G_G$ , is steadily increased above 1.20 Å into the region for potential  $O_2$ -ring interactions and along both channels, being more than enough to allow the passage of  $O_2$  and even a water molecule<sup>55,58</sup> (Figure 5). The tunnels in both mutants are most sterically favorable for the passage of dioxygen with respect to the hWT counterpart.

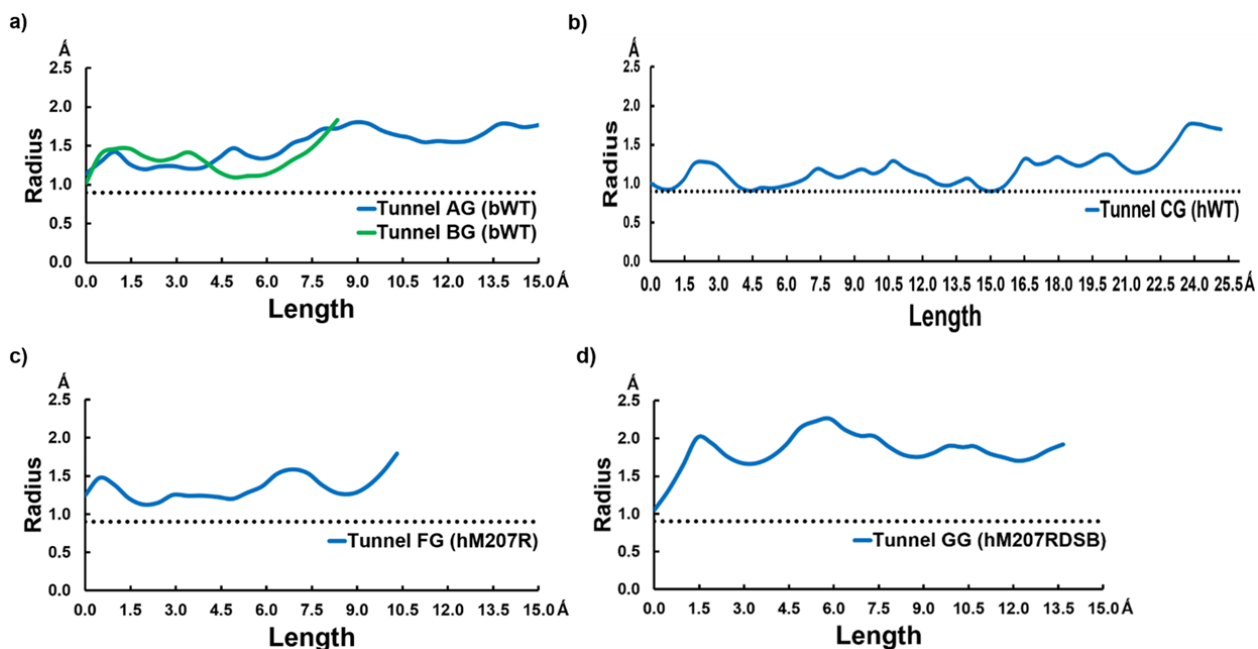


**Figure 5.** Tunnel radius, Angstroms ( $\text{\AA}$ ), as a function of the trajectory length in  $\text{\AA}$ : a) tunnels  $A_G$  and  $B_G$  in bWT, b) tunnel  $C_G$  in hWT, c) tunnel  $F_G$  in hM207R, and d) tunnel  $G_G$  in hM207R<sub>DSB</sub>. The line under the curve represents the probe radius of  $0.9 \text{ \AA}$  used for the calculations with the CAVER algorithm. The origin  $(0,0)$  corresponds to the starting point to the VD-tunnel search at  $3.0 \text{ \AA}$  from the  $\beta$ -ionone ring (into the collision sphere for potential  $O_2$ -ring interactions) and the final length value is defined by coordinates accessible to the aqueous solvent.

*Energetic viability of  $O_2$  migration pathways toward the  $\beta$ -ionone ring.* The  $\Delta G_{O_2-RHO}$  values along pathways A and B in bWT, show that  $O_2$  can migrate from the bulk solvent to the  $\beta$ -ionone ring (through the routes  $A_E$  and  $B_E$ ), since the free energy barrier is sufficiently low ( $< 6.0 \text{ kcal/mol}$ ), Figure 6. In fact, studies state that protein regions with the lowest barrier of  $6.4$  and  $7.5 \text{ kcal/mol}$  are crossed by dioxygen, being large barriers those that are in the range  $10 - 20 \text{ kcal/mol}$ <sup>51,124</sup>.

The highest energy barriers — the difference between the lowest and highest  $\Delta G$  value — are  $1.13$  and  $1.28 \text{ kcal/mol}$  in the direction from solvent to  $\beta$ -ionone ring, as well as  $2.15$  and  $2.10 \text{ kcal/mol}$  for the gas molecule to travel from the retinal ring to the solvent along the paths  $A_E$  and  $B_E$ , respectively. The maximum energy values for these routes are  $0.66$  ( $A_E$ ) and  $0.49$  ( $B_E$ )  $\text{kcal/mol}$  (Figure 6). Thus, the FEP calculations indicate that the molecular oxygen would not find a

significant energetic hindrance to migrate in both directions (solvent ring), with O<sub>2</sub> migration from the water solution to the  $\beta$ -ionone ring being most favourable.

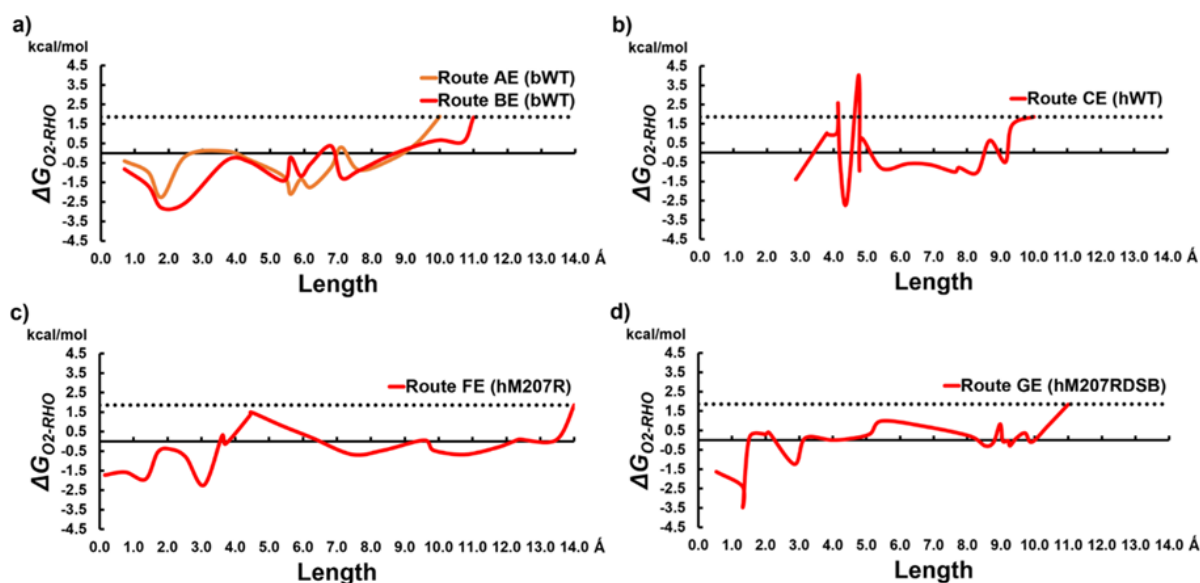


**Figure 6.** Free energy, in kcal/mol, profiles for the migration of molecular oxygen along the length, in Angstroms (Å), of the trajectory between starting points accessible to the solvent on the protein surface (final length values) and ending coordinates (origin  $0,0$ ) at 3.0 Å from the mass center of the  $\beta$ -ionone ring of retinal. a) routes A<sub>E</sub> and B<sub>E</sub> in bWT; b) route C<sub>E</sub> in hWT; c) route F<sub>E</sub> in hM207R; and d) route G<sub>E</sub> in hM207R<sub>DSB</sub>. The free energies are calculated from the O<sub>2</sub>-PMF values computed by using the ILS method. The line above each curve corresponds to the calculated free energy for O<sub>2</sub> solvation into the aqueous system part.

For hWT, the lowest-energy O<sub>2</sub> route C<sub>E</sub> is identified at the H5 – H6 gate between the same endpoints used for the bWT system (Figures 4, 6, and S7). Nevertheless, the migration of dioxygen toward the  $\beta$ -ionone moiety is much less favorable (or unviable) in hWT. The route C<sub>E</sub> exhibits the closer minimum to the retinal at  $\sim 2.0$  and  $5.0$  Å away from the collision sphere and the mass center of the  $\beta$ -ionone moiety, respectively, and so does not allow that dioxygen reaches the retinal ring inside hWT. Moreover, the coordinates of C<sub>E</sub> do not match those of the geometrical VD tunnel C<sub>G</sub>. In addition, C<sub>E</sub> exhibits the highest energy barriers in both the solvent  $\rightarrow$   $\beta$ -ionone ring (4.88 kcal/mol) and  $\beta$ -ionone ring  $\rightarrow$  solvent (6.60 kcal/mol) direction. The maximum energy value along the FEP experienced by dioxygen traveling through the route C<sub>E</sub> is 4.02 kcal/mol (Figures 4

and 6). Even though, the O<sub>2</sub> migration is also easier in direction to the retinal ring for hWT, the lowest-energy path C<sub>E</sub> has the highest energetic barrier among all analyzed systems. The high-energy cost of the tunnel C<sub>E</sub> is expected due to the highest steric hindrance identified for the tunnel C<sub>G</sub> in the same region of the hWT model (Table 1; Figures 5 and 6).

In the hM207R mutant rhodopsins, the top geometrical tunnel—with the highest throughput—F<sub>G</sub> from cluster F<sub>GC</sub> is followed closely by the energy-enabled route F<sub>E</sub> for migration of O<sub>2</sub> through a nonpolar microenvironment defined by residues at the H6 – H7 gate. Similarly, for hM207R<sub>DSB</sub>, a high spatial correspondence is found between the lowest-energy pathway G<sub>E</sub> and the trajectory of the top tunnel G<sub>G</sub> (from cluster G<sub>GC</sub>) passing over hydrophobic residues located at the H5 – H6 gate (Figures 4 and S7).

In comparison to hWT, the routes F<sub>E</sub> and G<sub>E</sub> exhibit the lowest and most permissive energy barriers of 1.44 and 1.63 kcal/mol for the migration of O<sub>2</sub> to the retinal ring inside the hM207R and hM207R<sub>DSB</sub> systems, respectively. Both routes end at the lowest energy values calculated near the retinal ring (–1.72 kcal/mol for hM207R and –1.64 kcal/mol for hM207R<sub>DSB</sub>). In the mutants, the migration of molecular oxygen toward the β-ionone moiety is also more favorable than to the opposite direction for which the energy-barrier values are 2.53 (hM207R) and 3.53 (hM207R<sub>DSB</sub>) kcal/mol. The highest values of free energy of the FEP corresponding to the routes F<sub>E</sub> and G<sub>E</sub> along the polypeptide matrixes are 1.49 kcal/mol and 0.98 kcal/mol, respectively (Figure 6).

An approach based only on the  $\Delta G_{O_2-ring}$  value is less realistic by neglecting in the analysis possible earlier contacts of the outmost atoms of the retinal ring with a molecule of O<sub>2</sub> before eventually entering to a region defined by the minimum and maximum coordinates of the box containing it. However, the free energy cost of placing dioxygen, into the closest region to the β-ionone ring inside bWT ( $\Delta G_{O_2-ring} = 0.38$  kcal/mol), is lower than the solvation free energy of the gas molecule

in water (Table 2). Therefore,  $\Delta G_{O_2-ring}$  also indicates that the O<sub>2</sub> migration is possible from the solvent to even more internally within the probable collision sphere containing the retinal ring into the bovine-WT RBP. The solvation free energy of dioxygen in water ( $\Delta G_{O_2-solv}$ ) of 1.85 kcal/mol calculated here is in agreement with both the experimental value of 1.78 kcal/mol obtained at 20 °C<sup>129</sup> and a theoretical value of 1.97 kcal/mol reported previously<sup>48,103</sup>.

The average  $\Delta G_{O_2-ring}$  value obtained for hWT (1.94 kcal/mol) is 1.56 kcal/mol higher than that for bWT, being also the highest value exceeding  $\Delta G_{O_2-solv}$  slightly (Table 2). Thus, the lowest probability to find O<sub>2</sub> near the retinal ring corresponds to hWT. A  $\Delta G_{O_2-ring}$  value lower than  $\Delta G_{O_2-solv}$  would not improve the arrival of dioxygen to the  $\beta$ -ionone ring due to the energetic unviability of the pathway C<sub>E</sub> to transport the gas molecule to regions occupied by retinal inside the hWT rhodopsin structure (Table 2; Figure 4).

The free energy profiles of the routes F<sub>E</sub> and G<sub>E</sub> as well as the geometrical characterization of the tunnels F<sub>G</sub> and G<sub>G</sub> show that the  $\beta$ -ionone ring is accessible to the molecular oxygen coming from the aqueous solvent in both structures of the M207R mutant. In agreement with this finding, the  $\Delta G_{O_2-ring}$  values of -0.07 (hM207R) and -0.77 (hM207R<sub>DSB</sub>) kcal/mol, indicate that the probability of finding dioxygen at the rhodopsin binding site (most specifically at the region closest to the retinal ring) is higher for the mutant rhodopsin (Table 2). In fact, the  $\Delta G_{O_2-ring}$  values are much lower than  $\Delta G_{O_2-solv}$  for these mutant systems, which is congruent with a more favorable O<sub>2</sub> migration from the solvent to the retinal ring, as shown by the FEP calculations (Table 2; Figure 6).

By mapping the network of potential O<sub>2</sub> pathways through the computed iso-energy surfaces of the PMF at the contour values of -1.0 and 1.0 kT, the  $\beta$ -ionone ring is identified as the retinal



moiety most accessible to the gas molecule at the RBP inside all analyzed rhodopsin structures (Figure 7).

The iso-energy surfaces of the O<sub>2</sub>-PMF map computed by ILS calculations for bWT rhodopsin, delimit regions around the retinal ring with high probability of finding O<sub>2</sub> in the contour value range  $-1.0 - 1.0$  kT (Figures 7 and S5), congruently with the prediction reported by a previous theoretical study<sup>25</sup>. However, the rest of the bWT RBP appears much less permeable to molecular oxygen (Figure 7). The probability of transferring an oxygen molecule from the vacuum to any region of the RBP is notably reduced in this system (Figures 7 and S5). Again, the O<sub>2</sub>-PMF maps indicate that the migration of dioxygen is highly unlikely from the water solution to the  $\beta$ -ionone ring region and other regions of the RBP inside the hWT rhodopsin. These findings are in agreement with experimental observations that state a certain level of protection of the RBP against the inclusion of dioxygen in bWT rhodopsin<sup>35</sup>.

**Table 2. Free energy ( $\Delta G_{O_2-ring}$ ) of placing O<sub>2</sub> into the nearest region to the  $\beta$ -ionone ring of retinal inside the bWT, hWT, hM207R and hM207R<sub>DSB</sub> structural models.**

Structure	$\Delta G_{O_2-ring}^*$
bWT	0.38
hWT	1.94
hM207R	-0.07
hM207R <sub>DSB</sub>	-0.77

\*Average free energy values (in kcal/mol) obtained from PMF values computed for a box that is defined by the minimum and maximum coordinates of the  $\beta$ -ionone ring into the rhodopsin binding pocket each structure, using the ILS method on 5000 simulation frames from the equilibrated dynamic trajectory.

The highest number and the largest extension of favorable regions to place O<sub>2</sub> in the vicinity of the  $\beta$ -ionone ring are found in the mutant structures (with a higher number of energy minima identified in the hM207R<sub>DSB</sub> system, Figures 7 and S5). The iso-energy surface of the O<sub>2</sub>-PMF in the rhodopsins shows that oxygen permeability is increased in the mutant RBP with respect to the

counterpart site in the hWT rhodopsin, according to the FEP and  $\Delta G_{O_2\text{-ring}}$  calculations described previously (Table 2; Figures 6, 7, and S5).

The geometric-energetic analysis shows that the viability of the  $O_2$  migration, between the  $\beta$ -ionone and bulk solvent, increases when going from hWT to bWT, hM207R and hM207R<sub>DSB</sub> systems. The steric and energetic characteristics identified for each tunnel or route of  $O_2$  show that the retinal binding site could be the most protected, or even impermeable, to  $O_2$  in the human visual pigment. In fact, as expected, average heavy-atom hydrogen bond distances reveal significant hydrogen bond network perturbations around the 11-*cis*-retinal in the rhodopsin binding pocket in both M207R mutant variants compared with the hWT model (Table S2, Supporting Information).

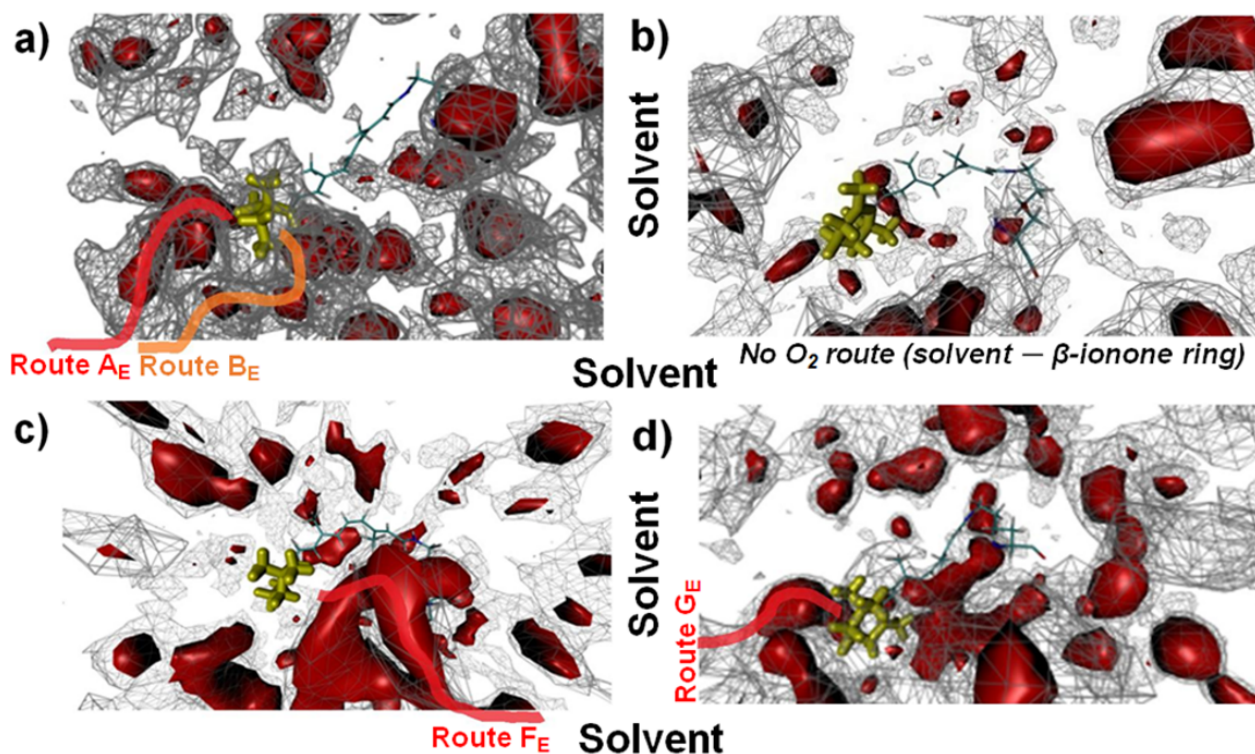


**Figure 7.**  $O_2$ -PMF isosurfaces at the contour values -1.0 (in red solid) and 1.0 (in gray wireframe) kT for the retinal binding pocket of equilibrated rhodopsin structures embedded in a water box: a) bWT; b) hWT; c) hM207R; and d) hM207R<sub>DSB</sub>. Red or orange transparent lines are placed on the most favorable region crossed by the routes A<sub>E</sub>, B<sub>E</sub>, F<sub>E</sub> or G<sub>E</sub> into the network of  $O_2$  pathways inside each rhodopsin. Schematically, the trajectory of each route is drawn from the solvent (out of the iso-energy surface representation) to the  $\beta$ -ionone ring (in yellow licorice). Both Lys296 and the rest of the 11-*cis*-retinal structure are in licorice representation coloured by atom types.

The analyses are coincident in that the retinal ring is more accessible to O<sub>2</sub> in both M207R-mutant variants with respect to the hWT counterpart (Figures 4-7, S5 and S7).

Here, putative migrations of O<sub>2</sub> are described inside human rhodopsins for the first time, which will help to address not only current questions of the availability of O<sub>2</sub> at the retinal binding pocket for photosensitizing reactions but also the accessibility of the singlet oxygen to the chromophore. The latter could also be relevant for understanding the *cis*–*trans* isomerization, molecular events in retinal degenerations, and optogenetics applications<sup>25</sup>.

***Identifying photosensitizing energetic potentialities of 11-cis-retinal in rhodopsins embedded within water solution.*** We determined average QM/MM energies associated with photosensitizing potentialities of 11-*cis*-retinal in the protein environment of the WT and mutant rhodopsins. Previous electron density analyses (using a similar QM/MM protocol) showed that both the conjugated electronic  $\pi$  system and frontier molecular orbitals are placed on 11-*cis*-retinal at the RBP<sup>24,37</sup>. These findings are consistent with those describing the placement of HOMO and LUMO orbitals on retinal, even when it is embedded in rhodopsins adopting the dark state conformation<sup>113,130,131</sup>. The previous electron density analyses indicate the retinal as the responsible chromophore of the light energy absorption into the QM region in WT and mutant M207R rhodopsins. Therefore, the QM/MM energies described in this work are obtained using the complete structure of 11-*cis*-retinal into the RBP due to its highly conjugated electronic configuration<sup>24</sup>.

***Excess energy in the retinal binding site of rhodopsins embedded in water after photoabsorption.*** The 11-*cis*-retinal is the chromophore determining an intensive light absorption at ~500 nm in bWT and hWT rhodopsins<sup>13,67-69</sup>. The following simple analysis allows to identify that the excess

energy after absorption of a photon by the opsin-embedded retinal is very close to or above the excitation energy of singlet oxygen (22.5 kcal/mol<sup>10,11,132</sup>), in both the WT and M207R mutant rhodopsins. The assumption of the energy gap reported for the ground and the lowest energy excited electronic states of molecular oxygen is based on evidences of photosensitized O<sub>2</sub>(a<sup>1</sup>Δ<sub>g</sub>) production by hydrophobic residues carrying π-clouds inside proteins<sup>31</sup>. These experimental determinations state that the O<sub>2</sub> quenching rate constant is defined by the protein flexibility and the accessibility of the gas molecule to photosensitizer moieties in the polypeptide matrix instead of changes on O<sub>2</sub> properties inside proteins<sup>31</sup>.

In bWT- and hWT rhodopsins within lipidic membranes or in non-membrane environments, the energy absorbed ( $E_A$ ) of ca. 57 kcal/mol<sup>13,36,67-69,79,88</sup> exceeds the energy of rhodopsin light activation that ranges between 40 and 50 kcal/mol in vertebrate rods<sup>133</sup>, whereas the stored energy ( $E_s$ ) into the bathorhodopsin intermediate is in the range 32–35 kcal/mol<sup>134,135</sup>. Hence the difference between  $E_A$  (*i.e.*  $\lambda_{\max}$ , VEE,  $\Delta E_{S_I-S_0}$ , or  $S_I$ -state energy) and  $E_s$  (32–35 kcal/mol) leads to minimum- and maximum-excess energies of 22 and 25 kcal/mol, respectively, in these WT rhodopsins.

In the M207R mutant rhodopsin structures, the bulkier positively charged group of Arg207 is placed into the RBP region near the β-ionone ring of the retinal chain (Figures 2 and 4), inducing a large spectral blue shift leading to  $E_A$  values of 4 and 18 kcal/mol higher with respect to both WT rhodopsins<sup>24,36,37,71</sup>. The absorption coefficient is also high for the wavelength of the blue-shifted excitation light in the M207R mutant<sup>36</sup>. On the other hand, the wavelength dependence of the retinal *cis*–*trans* isomerization does not occur when the blue–shifting effect is below 500 nm<sup>136</sup>. Therefore, the significant spectral blue shift observed in the M207R mutant<sup>36,37</sup> would not disturb the retinal isomerization process that could compete with the O<sub>2</sub> quenching. Nevertheless, non-optimum retinal conformation for the photoisomerization reaction has been reported for the

M207R mutant<sup>24</sup>. Either way, the excess energies can range from 26 to 45 kcal/mol, according to the subtraction between minimum/maximum  $E_A$  and  $E_s$  values, even when the endothermicity in the M207R-mutant structure is similar to that of the bathorhodopsin-WT intermediate. The  $\Delta E_{T_1-S_0}$  values calculated for the QM regions of the bWT, hWT, hM207R, and hM207R<sub>DSB</sub> systems are higher than the excitation energy of  $O_2(a^1\Delta_g)$ , which indicate that it is possible to transfer energy from the  $T_1$  state of retinal to the ground state of dioxygen, at least from a thermodynamic standpoint (see Table 3).

The upper limit of the  $T_1$ -state energy of retinal has been established in 40 kcal/mol by experimental measurements with a retinal analogue out of the protein environment<sup>137,138</sup>. The calculated  $\Delta E_{T_1-S_0}$  values for the retinal inside all analyzed rhodopsins are reasonably between ca. 13.5 and 15 kcal/mol lower than that energy limit for retinoide triplets (Table 3).

**Table 3.  $T_1-S_0$  energy gap ( $\Delta E_{T_1-S_0}$ ) and approximated ionization potential ( $IP_{approx}$ ) related to the  $S_0$  state of 11-*cis*-retinal embedded in QM/MM optimized rhodopsin structures.**

System	$\Delta E_{T_1-S_0}^a$	$IP_{approx}^a$
bWT	$25.6 \pm 0.2$	$132.6 \pm 6.4$
hWT	$26.5 \pm 1.0$	$161.6 \pm 7.2$
hM207R	$25.0 \pm 2.3$	$154.1 \pm 6.9$
hM207R <sub>DSB</sub>	$26.3 \pm 2.1$	$144.4 \pm 5.3$

<sup>a</sup>Energy and  $IP_{approx}$  values are given in kcal/mol and correspond to average values over five snapshots.  $IP_{approx}$  is approximated as the negative of the HOMO energy at the  $S_0$  state. See Methods section for more details.

Several studies state that the intersystem crossing  $S_1 \rightarrow T_1$  occurs favorably between the retinal excited states in different environments, including its binding pocket in rhodopsins<sup>27-29,137,138</sup>. The  $O_2$  quenching of the  $S_1$  state can generate singlet oxygen and induce ISC when  $\Delta E_{S_1-T_1}$  is greater than the  $O_2(a^1\Delta_g)$ -excitation energy<sup>11,139</sup>. This deactivation process competes with the ultrafast 11-*cis*/all-*trans* isomerization reaction in the  $S_1$  state<sup>28</sup> that occurs on the femtosecond time scale (200

fs) in WT bovine rhodopsin, although the retinal isomerizes completely after a longer significant time window than 3.2 ps<sup>13</sup>. In fact, the photosensitized generation of O<sub>2</sub>(a<sup>1</sup>Δ<sub>g</sub>) is also an ultrafast and a diffusion-limited process depending on the collision between the excited photosensitizer and O<sub>2</sub><sup>44</sup>.

Although, studies describe the high efficiency (0.65) of the *cis-trans* retinal isomerization via S<sub>1</sub>/S<sub>0</sub> canonical intersection, their authors also state that the population of the T<sub>1</sub> state can be a possible deactivation path for this reaction after photoabsorption<sup>28,114</sup> or energy transfer<sup>26</sup>. Specifically, the 11-*cis*-retinal in solutions generate long-lived triplet states that interact with molecular oxygen and that produce singlet oxygen. In fact, the photosensitized generation of this reactive oxygen species has been used as indicative of the significant role of the 11-*cis*-retinal triplet states in the photoisomerization reaction<sup>28</sup>. These experimental results reveal that the photoisomerization from this triplet state has an efficiency of 1 ± 0.2, exhibiting that it is possible a significant quantitative isomerization via 11-*cis*-retinal triplet. Subsequently, this excited state evolves to all-*trans*-retinal triplet before being transformed to all-*trans* retinal (ground state). The excited triplet state of the β-ionone molecule has also been reported experimentally<sup>30</sup>. Moreover, theoretical results show that retinal isomerization in the rhodopsin binding pocket can be mediated by the lowest excited triplet state of the chromophore<sup>114</sup>. These evidences support that the triplet population of 11-*cis*-retinal can occur and be quenched by O<sub>2</sub> to yield O<sub>2</sub>(a<sup>1</sup>Δ<sub>g</sub>), being possible the implication of the β-ionone in this photosensitizing reaction.

According to the reported values of S<sub>1</sub>-state energy (*vide supra*) and the T<sub>1</sub>-state energy calculated for WT and M207R rhodopsins (Table 3), the resulting ΔE<sub>S<sub>1</sub>-T<sub>1</sub></sub> values are higher than 30 kcal/mol which is enough energy to generate O<sub>2</sub>(a<sup>1</sup>Δ<sub>g</sub>) from the lowest excited singlet state. Since the population of the T<sub>1</sub> state of retinal can be favored<sup>28,29,114,137,138</sup>, it is expected that the ISC rates

exceed the quenching of the  $S_1$  state being not much longer-lived than the  $T_1$  state. The longer the  $T_1$ -state lifetime of a photosensitizer, the higher the efficiency to produce  $O_2(a^1\Delta_g)$  when its corresponding  $\Delta E_{T_1-S_0}$  value exceeds 22.5 kcal/mol<sup>10,11</sup>. Thus, the triplet-triplet energy transfer from the previously light-excited retinal to  $O_2$  would be highly probable in exothermic conditions to generate  $O_2(a^1\Delta_g)$  and to compete with the photoisomerization of the chromophore during the multiplicity change, being also possible the quenching of the excited triplet state of 11-*cis*-retinal by  $O_2$ . This assumption is in agreement with experimental results obtained by Feis *et al.*<sup>28</sup>. These authors demonstrated that the light-excited 11-*cis*-retinal, in aerated solutions, is able to generate long-lived triplet states, which are quenched by  $O_2$  to produce singlet oxygen with high quantum efficiency ( $\phi_\Delta = 0.27$  vs values of photoisomerization quantum efficiency,  $\phi_{PI}$ , that ranges between 0.12 and 0.25 in solution). As also mentioned above, Borsarelli *et al.*<sup>30</sup> confirmed experimentally the formation of the excited triplet state of the  $\beta$ -ionone molecule acting as a precursor for the photosensitized production of singlet oxygen with a  $\phi_\Delta$  value of 0.16.

Recently, Valentini *et al.*<sup>26</sup> reported a QM/MM study focused on the feasibility of retinal isomerization mediated by the photosensitized lowest-lying triplet of the chromophore embedded in bovine rhodopsin. The study suggests that this pathway of retinal isomerization is less efficient with respect to the *cis-trans* photoisomerization of the singlet. These authors also assessed the energy conditions for the production of photosensitized  $O_2(a^1\Delta_g)$  from this retinal triplet state and propose that this reaction hardly contributes to retinal deactivation. The energy of the retinal triplet, in that study, corresponds to one conformation of minimum obtained by scanning an internal dihedral coordinate of the twist around the C11=C12 bond. Yet, the reported potential energy surface of this scan appears very flat for the triplet close to the minimum, but not for the corresponding ground states. Hence, one would expect the system to be able to explore this type

of deactivation also at higher energies that exceed the singlet-triplet oxygen gap. Further theoretical and experimental works are required to draw conclusions about the efficiency of photosensitization at the RBP. In addition, the  $O_2(a^1\Delta_g)$  generation by quenching the retinal  $S_1$ -state would not be ruled out either because of the  $S_1$ - $T_1$  band gap and the  $S_1$ -state energy of this chromophore that can be higher than the excitation energy of  $O_2(a^1\Delta_g)$ , especially for the analyzed mutant rhodopsins exhibiting a significant spectral blue shift. On the other hand, the conformation of retinal embedded in these perturbed visual pigments could lead to an inefficient isomerization reaction<sup>24</sup> to compete with an eventual and favorable photosensitization at the RBP. Therefore, photosensitizing reactions at blue-shifted mutant rhodopsin cores hosting retinal could not be a marginal process.

Although experimental results state that several retinal isomers, including 11-*cis*-retinal, can efficiently produce  $O_2(a^1\Delta_g)$  in aqueous solution upon light absorption<sup>28,140</sup>, it is not yet known which part of the retinal molecule is primarily responsible. The generation of the singlet  $O_2(a^1\Delta_g)$  through photosensitization is a diffusion-limited process<sup>44</sup>, faster than the likely timescale of (large scale) protein conformational changes. These observations evidence that even in polar media, the  $T_1$  states of the isomer 11-*cis*-retinal have sufficient lifetimes to be quenched by  $O_2$ , leading to photosensitization reactions (Type II). Therefore, the  $O_2$  quenching of these excited  $S_1$  and  $T_1$  states of retinal can be thermodynamically viable to induce photosensitized oxidation reactions into the RBP of the analyzed WT and mutant rhodopsins.

*Approximation to the ionization potential related to retinal inside water-solubilized rhodopsins.*

In rhodopsins, the conjugated  $\pi$  system of 11-*cis*-retinal leads to  $\pi\pi^*$  transitions during the excitation by visible light<sup>24,37</sup> and the retinal isolation by a protonated Schiff-base linked at the RBP<sup>13,24,36-38</sup> can prevent aggregation and aqueous solvation phenomena. These retinal



characteristics can reduce the chromophore reactivity, extending the  $T_1$ -state lifetimes of retinal at the RBP for  $O_2$  quenching. In fact, a low chemistry reactivity is expected from non-aggregating compounds with high oxidation potential (or high ionization potential) in non-aqueous solvation medium<sup>10,11,141</sup>.

The approximation to the ionization potential through the Koopmans formalism<sup>119</sup> shows that  $IP_{approx}$  values related to retinal in the QM region are lower in bWT, hM207R, and hM207R<sub>DSB</sub> rhodopsins than in the human WT counterpart (Table 3). Nevertheless, it would be expected a similar behavior between  $IP_{approx}$  values calculated for WT rhodopsins since they are obtained from equal QM-optimization settings for the ground states of retinal inside these structures with high compositional similarity in their binding sites<sup>37</sup>. In addition, as discussed above, the excited  $S_1$ - and  $T_1$ -state energies of the WT systems are not significantly different.

The conserved OE2<sub>Glu113</sub> – NZ<sub>Lys296</sub> salt bridge in both WT RBPs can explain the high correspondence between the energy of excited states, as the counterion Glu113 is a crucial determinant of the rhodopsin spectral properties<sup>32,142</sup> (Table S2, Supporting Information). On the other hand, the  $IP_{approx}$  values could be more sensitive to the conformational changes taking place in the rest of the bovine RBP, especially in the region closer to the  $\beta$ -ionone ring (Figure S10, Supporting Information). Congruently with these conformational differences, the  $O_2$  migration was more favorable to the cyclohexenyl moiety of retinal in bWT than in hWT (where the RBP is more protected against  $O_2$  penetration, *vide supra*). The placement of the frontier orbitals on the 11-*cis*-retinal of the systems investigated here<sup>37</sup>, leave no doubt that the  $IP_{approx}$  calculation is an appropriate comparative approximation to that redox property of the chromophore into the RBP. In bWT and M207R mutant rhodopsins, the lower  $IP_{approx}$  value associated with the electronic configuration of the ground state of 11-*cis*-retinal, indicate the decrease of the ionization potential

with respect to hWT (Table 3). The lower the ionization potential of a compound, the easier the oxidation which would be reflected in its lower oxidation potential ( $E_{ox}$ ).

Previous works conclude that a decreased  $E_{ox}$  of the sensitizer leads systematically to an increment in the rate constants for  $O_2$  quenching of lowest excited singlet ( $k_{S_1^Q}$ ) and triplet states ( $k_{T_1^Q}$ ) of sensitizers, and to a decrease in the quantum efficiency ( $S_A$ ) of the latter to generate  $O_2(a^1\Delta_g)^{10}$ . Under this reasoning, compared to hWT rhodopsin, the singlet oxygen formation can become faster from  $S_1$  and  $T_1$  states related to 11-*cis*-retinal embedded into bWT, hM207R, and hM207R<sub>DSB</sub> rhodopsins (Table 3). In fact, a charger-transfer (CT) long-lived complex can be formed by sensitizers exhibiting an ionization potential lower than 207.5 kcal/mol with little variation of  $k_{S_1^Q}$  values, which leads to a complete  $O_2$  quenching<sup>10</sup>. Therefore, it would be expected a weaker CT complex stabilization leading to an incomplete  $O_2$  quenching of  $S_1$  state in the hWT system. A higher  $k_{S_1^Q}$  value make more favorable (faster) the photosensitized  $O_2(a^1\Delta_g)$  production competing with the fast 11-*cis*/*all-trans* isomerization reaction in the  $S_1$  state<sup>28</sup>. Regardless of  $S_A$  behavior, a viable and fast photosensitizing reaction in RBP can lead to undesired and destructive oxidations affecting the structure and function of rhodopsins.

The photosensitizing reactions in the RBP of both WT rhodopsins would not be discarded from the energetic standpoint (Table 3). However, a photosensitizing activity would not be probable in the retinal binding site of hWT due to the absence of dioxygen near the known photosensitizer  $\beta$ -ionone ring<sup>30</sup>. On the other hand, the photosensitized  $O_2(a^1\Delta_g)$  production by the opsin-embedded retinal can be possible for dark-state conformations of bWT, hM207R, and hM207R<sub>DSB</sub> structures under these considerations. In comparison to hWT rhodopsin, our calculations predict that the 11-*cis*-retinal can be quenched by  $O_2$  to generate  $O_2(a^1\Delta_g)$  into the RBP perturbed by the M207R substitution linked to RP.

The cutoff wavelengths of the lens in the range 300 – 400 nm for young primates<sup>15,16,21</sup> can prevent that O<sub>2</sub> quenches excited aromatic residues<sup>31</sup> lining pathways of migration of the gas molecule in the analyzed rhodopsins. Nevertheless, the anterior segment of the eye allows that the light exciting the chromophore retinal (406 – 469 nm) impacts retina in M207R mutants. Both phenomena can contribute to the availability of O<sub>2</sub> migrating through predicted pathways toward the  $\beta$ -ionone ring and of enough excited-state energy upon retinal excitation into the less protected RBP of M207R mutants against such photosensitizing inputs. Since the intracellular action sphere of O<sub>2</sub>(a<sup>1</sup> $\Delta_g$ ) is larger than 20 nm<sup>11</sup>, and can alter protein structures<sup>143</sup>, a photosensitized singlet-oxygen generation by retinal could lead to significant irreversible changes into the RBP structure inside the RP-linked mutant-M207R rhodopsin. The O<sub>2</sub> pathways described in this work for rhodopsins can also be the passage of the reactive and destructive O<sub>2</sub>(a<sup>1</sup> $\Delta_g$ ) toward the RBP after being generated by other photosensitizing reactions with implication in physiological, pathological or technological processes. In these contexts, an oxidant microenvironment, caused by this kind of ROS in the pathological scenario of RP associated with less stable mutant rhodopsins, may lead to consider therapies that are based on flavonoid allosteric modulation of structurally perturbed rhodopsins. This therapy proposes the use of flavonoids that can act as allosteric modulators and increase both the antioxidant potential and the stability of mutant visual pigments<sup>144</sup>. In addition, the finding that photosensitizing properties of retinal can be modified in protein environments may be used to design photosensitizing rhodopsin-like tags in optogenetics<sup>43-45</sup>.

## CONCLUSIONS

In this work, simulations indicate a loss of protection against the penetration of molecular oxygen at the retinal binding site in the M207R mutant of human rhodopsin (regardless of the protonation

state of the Schiff base). The  $\beta$ -ionone ring is the region most accessible to dioxygen. After photoabsorption, the protein core with retinal bound can host enough energy to photosensitize  $O_2$  in the WT and M207R mutant rhodopsins. A photosensitized oxidation reaction is unlikely in the WT human rhodopsin because of structural protection against the migration of dioxygen toward the retinal ring. However, our findings suggest that photosensitizing reactions cannot be ruled out in the water-solubilized bovine-WT rhodopsin in terms of the accessibility of  $O_2$  to the  $\beta$ -ionone moiety and of the excited-state energy due to retinal light excitation in comparison with the human counterpart.

The blue-light absorbing M207R-mutant rhodopsins exhibit energies of the lowest excited triplet-states that are similar to those found for the WT human rhodopsin absorbing at  $\sim 500$  nm, which lead to larger excited-state singlet-triplet energy gaps in mutants with or without protonated Schiff base. The HOMO-energy analysis shows significant electronic configuration changes associated with the ground state of retinal within the M207R-mutant cores that can lead to a decrease of the chromophore ionization potential. Consequently, the  $O_2$  quenching of the retinal excited states could lead to faster generation of  $O_2(a^1\Delta_g)$  in the rhodopsin binding pocket due to the M207R substitution linked to *retinitis pigmentosa*. Possible pathways for  $O_2$  access to the  $\beta$ -ionone ring and excited-state energies of rhodopsin cores hosting the retinal chromophore are found in good agreement with available experimental and theoretical data, which may help to understand the viability and destructive effects of photosensitized oxidation reactions in visual pigments.

These findings reveal the photosensitizing potential of 11-*cis*-retinal embedded into water-solubilized mutant rhodopsins, as well as the possible accessibility of singlet oxygen to their protein cores, which could be associated with molecular mechanisms of retinal degenerations. Our results also show that an amino acid substitution can modify the photosensitizing properties

associated with retinal inside a photoactive protein. This indicates that rhodopsins could be (re)designed rationally and applied as blue-light-absorbing markers that generate single oxygen. Finally, we encourage that further theoretical and experimental studies are needed to get insights into the efficiency of photosensitization reactions at blue-shifted mutant rhodopsin cores hosting retinal.

## **AUTHOR INFORMATION**

### **Corresponding Author**

\*E-mail: [ehernandez@ucm.cl](mailto:ehernandez@ucm.cl)

### **ORCID**

Erix W. Hernández-Rodríguez: <https://orcid.org/0000-0002-9231-7552>

Andrés M. Escorcía: <https://orcid.org/0000-0002-6498-4817>

Marc W. van der Kamp: <https://orcid.org/0000-0002-8060-3359>

Ana L. Montero-Alejo: <https://orcid.org/0000-0003-1675-0546>

Julio Caballero: <https://orcid.org/0000-0003-0182-1444>

### **Author Contributions**

E.W.H.R. and A.L.M.A. conceived the general idea of the investigation. E.W.H.R. performed the MD simulations, implicit ligand sampling, and Voronoi diagram calculations. E.W.H.R. and A.E. designed and performed the QM/MM calculations. E.W.H.R., A.E., and A.L.M.A. wrote the manuscript. M.W.v.d.K. and J.C. supervised the work and helped with the paper writing. All authors have given approval to the final version of the manuscript.

### **Funding Sources**

Authors E.W.H.R., J.C., and A.L.M.A. received funding from the Chilean “Fondo Nacional de Desarrollo Científico y Tecnológico” (FONDECYT) Grants 3170107, 1170718, and 11180984,

respectively. A.E. and M.W.v.d.K. received funding from BBSRC, Grant numbers BB/M026280/1 & BB/R001332/1.

## Notes

The authors declare no conflict of interest.

The authors declare no competing financial interest.

## ACKNOWLEDGMENT

E.W.H.R. and J.C. thank CONICYT FONDECYT/INACH/POSTDOCTORADO/No. 3170107. A.E. and M.W.v.d.K. thank BBSRC for funding (Grant numbers BB/M026280/1 & BB/R001332/1). A. L. M. A. is thankful for a CONICYT/FONDECYT Iniciación 11180984 grant and to Núcleo Milenio MULTIMAT, Chile. The Centro de Bioinformática y Simulación Molecular at the Universidad de Talca and Universidad Católica del Maule were the main host institutions for this work. The Advanced Computing Research Centre of the University of Bristol provided additional computational facilities.

## REFERENCES

1. Bales, K.L.; Ianov, L.; Kennedy, A.J.; Sweatt, J.D.; Gross, A.K. Autosomal Dominant Retinitis Pigmentosa Rhodopsin Mutant Q344X Drives Specific Alterations in Chromatin Complex Gene Transcription. *Mol. Vis.* **24**, 153 (2018).
2. Martin-Merida, I.; Aguilera-Garcia, D.; Fernandez-San Jose, P.; Blanco-Kelly, F.; Zurita, O.; Almoguera, B.; Garcia-Sandoval, B.; Avila-Fernandez, A.; Arteché, A.; Minguez, P. Toward the Mutational Landscape of Autosomal Dominant Retinitis Pigmentosa: A Comprehensive Analysis of 258 Spanish Families. *Invest. Ophthalmol. Vis. Sci.* **59**, 2345-2354 (2018).
3. Artero Castro, A.; Lukovic, D.; Jendelova, P.; Erceg, S. Concise Review: Human Induced Pluripotent Stem Cell Models of Retinitis Pigmentosa. *Stem Cells* **36**, 474-481 (2018).
4. Organisciak, D.T.; Darrow, R.M.; Barsalou, L.; Kutty, R.K.; Wiggert, B. Susceptibility to Retinal Light Damage in Transgenic Rats with Rhodopsin Mutations. *Invest. Ophthalmol. Vis. Sci.* **44**, 486-492 (2003).
5. Chen, Y.; Perusek, L.; Maeda, A. Autophagy in Light-Induced Retinal Damage. *Exp. Eye Res.* **144**, 64-72 (2016).

6. Kruk, J.; Kubasik-Kladna, K.; Y Aboul-Enein, H. The Role Oxidative Stress in the Pathogenesis of Eye Diseases: Current Status and a Dual Role of Physical Activity. *Mini-Rev. Med. Chem.* **16**, 241-257 (2016).
7. Hammond, B.R.; Johnson, B.; George, E.R. Oxidative Photodegradation of Ocular Tissues: Beneficial Effects of Filtering and Exogenous Antioxidants. *Exp. Eye Res.* **129**, 135-150 (2014).
8. Zhou, Y.Y.; Chen, C.Z.; Su, Y.; Li, L.; Yi, Z.H.Z.; Qi, H.; Weng, M.; Xing, Y.Q. Effect of EGb761 on Light-Damaged Retinal Pigment Epithelial Cells. *Int. J. Ophthalmol.* **7**, 8 (2014).
9. Demmig-Adams, B.; Adams, R.B. Eye Nutrition in Context: Mechanisms, Implementation, and Future Directions. *Nutrients* **5**, 2483-2501 (2013).
10. Schweitzer, C.; Schmidt, R. Physical Mechanisms of Generation and Deactivation of Singlet Oxygen. *Chem. Rev.* **103**, 1685-1757 (2003).
11. Ogilby, P.R. Singlet Oxygen: There Is Indeed Something New under the Sun. *Chem. Soc. Rev.* **39**, 3181-3209 (2010).
12. Orban, T.; Jastrzebska, B.; Palczewski, K. Structural Approaches to Understanding Retinal Proteins Needed for Vision. *Curr. Opin. Cell Biol.* **27**, 32-43 (2014).
13. Menon, S.T.; Han, M.; Sakmar, T.P. Rhodopsin: Structural Basis of Molecular Physiology. *Physiol. Rev.* **81**, 1659-1688 (2001).
14. Chamorro, E.; Bonnin, C.A.; Pérez, M.J.C.; Luna, J.M.; Vázquez, D.; Sánchez, C.R. Effects of Light-Emitting Diode Radiations on Human Retinal Pigment Epithelial Cells *in Vitro*. *Photochem. Photobiol.* **89**, 468-473 (2013).
15. Mainster, M.A. Violet and Blue Light Blocking Intraocular Lenses: Photoprotection Versus Photoreception. *Br. J. Ophthalmol.* **90**, 784-792 (2006).
16. Glickman, R.D. Ultraviolet Phototoxicity to the Retina. *Eye & Contact Lens* **37**, 196-205 (2011).
17. Grimm, C.; Wenzel, A.; Hafezi, F.; Yu, S.; Redmond, T.M.; Remé, C.E. Protection of Rpe65-Deficient Mice Identifies Rhodopsin as a Mediator of Light-Induced Retinal Degeneration. *Nature Genet.* **25**, 63 (2000).
18. Hunter, J.J.; Morgan, J.I.W.; Merigan, W.H.; Sliney, D.H.; Sparrow, J.R.; Williams, D.R. The Susceptibility of the Retina to Photochemical Damage from Visible Light. *Prog. Retin. Eye Res.* **31**, 28-42 (2012).
19. Osborne, N.N.; Kamalden, T.A.; Majid, A.S.A.; del Olmo, S.A.; Manso, A.G.; Ji, D. Light Effects on Mitochondrial Photosensitizers in Relation to Retinal Degeneration. *Neurochem. Res.* **35**, 2027-2034 (2010).
20. van Norren, D.; Gorgels, T.G.M.F. The Action Spectrum of Photochemical Damage to the Retina: A Review of Monochromatic Threshold Data. *Photochem. Photobiol.* **87**, 747-753 (2011).
21. Rózanowska, M.; Sarna, T. Light-Induced Damage to the Retina: Role of Rhodopsin Chromophore Revisited. *Photochem. Photobiol.* **81**, 1305-1330 (2005).
22. Noell, W.K.; Walker, V.S.; Kang, B.S.; Berman, S. Retinal Damage by Light in Rats. *Invest. Ophthalmol.* **5**, 450-473 (1966).
23. Boulton, M.; Rózanowska, M.; Rózanowski, B. Retinal Photodamage. *J. Photochem. Photobiol. B: Biol.* **64**, 144-161 (2001).
24. Hernández-Rodríguez, E.W.; Montero-Alejo, A.L.; López, R.; Sánchez-García, E.; Montero-Cabrera, L.A.; García de la Vega, J.M. Electron Density Deformations Provide New Insights into the Spectral Shift of Rhodopsins. *J. Comput. Chem.* **34**, 2460-2471 (2013).
25. Marazzi, M.; Gattuso, H.; Giussani, A.; Zhang, H.; Navarrete-Miguel, M.; Chipot, C.; Cai, W.; Roca-Sanjuán, D.; Dehez, F.; Monari, A. Induced Night Vision by Singlet-Oxygen-Mediated Activation of Rhodopsin. *J. Phys. Chem. Lett.* **10**, 7133-7140 (2019).
26. Valentini, A.; Nucci, M.; Frutos, L.M.; Marazzi, M. Photosensitized Retinal Isomerization in Rhodopsin Mediated by a Triplet State. *ChemPhotoChem.* **3**, 925-932 (2019).
27. Röhrig, U.F.; Guidoni, L.; Laio, A.; Frank, I.; Rothlisberger, U. A Molecular Spring for Vision. *J. Am. Chem. Soc.* **126**, 15328-15329 (2004).

28. Feis, A.; Wegewijs, B.; Wolfgang, G.; Braslavsky, S.E. Role of the Triplet State in Retinal Photoisomerization as Studied by Laser-Induced Optoacoustic Spectroscopy. *J. Phys. Chem. B* **101**, 7620-7627 (1997).
29. Kiser, P.D.; Golczak, M.; Palczewski, K. Chemistry of the Retinoid (Visual) Cycle. *Chem. Rev.* **114**, 194-232 (2013).
30. Borsarelli, C.D.; Mischne, M.; Venia, A.L.; Vieyra, F.E.M. UVA Self-Photosensitized Oxygenation of  $\beta$ -Ionone. *Photochem. Photobiol.* **83**, 1313-1318 (2007).
31. Chin, K.K.; Trevithick-Sutton, C.C.; McCallum, J.; Jockusch, S.; Turro, N.J.; Scaiano, J.C.; Foote, C.S.; Garcia-Garibay, M.A. Quantitative Determination of Singlet Oxygen Generated by Excited State Aromatic Amino Acids, Proteins, and Immunoglobulins. *J. Am. Chem. Soc.* **130**, 6912-6913 (2008).
32. Okada, T.; Sugihara, M.; Bondar, A.N.; Elstner, M.; Entel, P.; Buss, V. The Retinal Conformation and Its Environment in Rhodopsin in Light of a New 2.2 Å Crystal Structure. *J. Mol. Biol.* **342**, 571-583 (2004).
33. *Protein Data Bank* (see [www.pdb.org](http://www.pdb.org)).
34. Cohen, J.; Schulten, K. O<sub>2</sub> Migration Pathways Are Not Conserved across Proteins of a Similar Fold. *Biophys. J.* **93**, 3591-3600 (2007).
35. Witold, K.S.; Geoffrey, E.R.; Rosalie, K.C.; James, S.H.; Akihiro, K. Oxygen Diffusion-Concentration Product in Rhodopsin as Observed by a Pulse ESR Spin Labeling Method. *Biophys. J.* **63**, 573-577 (1992).
36. Àguila, M.; Toledo, D.; Morillo, M.; Dominguez, M.; Vaz, B.; Alvarez, R.; de Lera, A.R.; Garriga, P. Structural Coupling of 11-*cis*-7-Methyl-Retinal and Amino Acids at the Ligand Binding Pocket of Rhodopsin. *Photochem. Photobiol.* **85**, 485-493 (2009).
37. Hernández-Rodríguez, E.W.; Sánchez-García, E.; Crespo-Otero, R.; Montero-Alejo, A.L.; Montero, L.A.; Thiel, W. Understanding Rhodopsin Mutations Linked to the Retinitis Pigmentosa Disease: A QM/MM and DFT/MRCI Study. *J. Phys. Chem. B* **116**, 1060-1076 (2012).
38. Rakoczy, E.P.; Kiel, C.; McKeone, R.; Stricher, F.; Serrano, L. Analysis of Disease-Linked Rhodopsin Mutations Based on Structure, Function, and Protein Stability Calculations. *J. Mol. Biol.* **405**, 584-606 (2011).
39. Li, Z.Y.; Kljavin, I.J.; Milam, A.H. Rod Photoreceptor Neurite Sprouting in Retinitis Pigmentosa. *J. Neurosci.* **15**, 5429-5438 (1995).
40. Athanasiou, D.; Aguila, M.; Bellingham, J.; Li, W.; McCulley, C.; Reeves, P.J.; Cheetham, M.E. The Molecular and Cellular Basis of Rhodopsin Retinitis Pigmentosa Reveals Potential Strategies for Therapy. *Prog. Retin. Eye Res.* **62**, 1-23 (2018).
41. Nemet, I.; Ropelewski, P.; Imanishi, Y. Rhodopsin Trafficking and Mistrafficking: Signals, Molecular Components, and Mechanisms. in *Prog. Mol. Biol. Transl.*, Vol. 132 39-71 (2015).
42. Athanasiou, D.; Aguilà, M.; Bevilacqua, D.; Novoselov, S.S.; Parfitt, D.A.; Cheetham, M.E. The Cell Stress Machinery and Retinal Degeneration. *FEBS Lett.* **587**, 2008-2017 (2013).
43. Westberg, M.; Bregnhøj, M.; Etzerodt, M.; Ogilby, P.R. No Photon Wasted: An Efficient and Selective Singlet Oxygen Photosensitizing Protein. *J. Phys. Chem. B* **121**, 9366-9371 (2017).
44. Losi, A.; Gardner, K.H.; Möglich, A. Blue-Light Receptors for Optogenetics. *Chem. Rev.* (2018).
45. Westberg, M.; Holmegaard, L.; Pimenta, F.M.; Etzerodt, M.; Ogilby, P.R. Rational Design of an Efficient, Genetically Encodable, Protein-Encased Singlet Oxygen Photosensitizer. *J. Am. Chem. Soc.* **137**, 1632-1642 (2015).
46. Kheitan, S.; Minuchehr, Z.; Soheili, Z.-S. Exploring the Cross Talk between ER Stress and Inflammation in Age-Related Macular Degeneration. *PLoS one* **12**, e0181667 (2017).
47. Audo, I.; Friedrich, A.; Mohand-Saïd, S.; Lancelot, M.-E.; Antonio, A.; Moskova-Doumanova, V.; Poch, O.; Bhattacharya, S.; Sahel, J.-A.; Zeitz, C. An Unusual Retinal Phenotype Associated with a Novel Mutation in Rho. *Arch. Ophthalmol.* **128**, 1036-1045 (2010).
48. Riedmayr, L.M.; Böhm, S.; Biel, M.; Becirovic, E. Enigmatic Rhodopsin Mutation Creates an Exceptionally Strong Splice Acceptor Site. *Hum. Mol. Genet.* **29**, 295-304 (2020).



49. Sosso, G.C.; Chen, J.; Cox, S.J.; Fitzner, M.; Pedevilla, P.; Zen, A.; Michaelides, A. Crystal Nucleation in Liquids: Open Questions and Future Challenges in Molecular Dynamics Simulations. *Chem. Rev.* **116**, 7078-7116 (2016).
50. Saxena, A.; Sangwan, R.S.; Mishra, S. Fundamentals of Homology Modeling Steps and Comparison among Important Bioinformatics Tools: An Overview. *Sci. Int* **1**, 237-252 (2013).
51. Cohen, J.; Arkhipov, A.; Braun, R.; Schulten, K. Imaging the Migration Pathways for O<sub>2</sub>, CO, NO, and Xe inside Myoglobin. *Biophys. J.* **91**, 1844-1857 (2006).
52. Pavelka, A.; Sebestova, E.; Kozlikova, B.; Brezovsky, J.; Sochor, J.; Damborsky, J. Caver: Algorithms for Analyzing Dynamics of Tunnels in Macromolecules. *Trans. Comput. Biol. Bioinform.* **13**, 505-517 (2016).
53. Cohen, J.; Olsen, K.W.; Schulten, K. Finding Gas Migration Pathways in Proteins Using Implicit Ligand Sampling. *Methods Enzymol.* **437**, 439-457 (2008).
54. Saam, J.; Ivanov, I.; Walther, M.; Holzhütter, H.-G.; Kuhn, H. Molecular Dioxygen Enters the Active Site of 12/15-Lipoxygenase Via Dynamic Oxygen Access Channels. *Proc. Natl. Acad. Sci. U. S. A.* **104**, 13319-13324 (2007).
55. Ebert, M.C.; Dürr, S.L.; Houle, A.; Lamoureux, G.; Pelletier, J.N. Evolution of P450 Monooxygenases toward Formation of Transient Channels and Exclusion of Nonproductive Gases. *ACS Catal.* **6**, 7426-7437 (2016).
56. Bustamante, J.P.; Szretter, M.E.; Sued, M.; Martí, M.A.; Estrin, D.A.; Boechi, L. A Quantitative Model for Oxygen Uptake and Release in a Family of Hemeproteins. *Bioinformatics* **32**, 1805-1813 (2016).
57. Boron, I.; Bustamante, J.P.; Davidge, K.S.; Singh, S.; Bowman, L.A.; Tinajero-Trejo, M.; Carballal, S.; Radi, R.; Poole, R.K.; Dikshit, K. Ligand Uptake in *Mycobacterium tuberculosis* Truncated Hemoglobins Is Controlled by Both Internal Tunnels and Active Site Water Molecules. *F1000Research* **4** (2015).
58. Collazo, L.; Klinman, J.P. Control of the Position of Oxygen Delivery in Soybean Lipoxygenase-1 by Amino Acid Side Chains within a Gas Migration Channel. *J. Biol. Chem.* **291**, 9052-9059 (2016).
59. Senn, H.M.; Thiel, W. QM/MM Methods for Biomolecular Systems. *Angew. Chem., Int. Ed.* **48**, 1198-1229 (2009).
60. Brunk, E.; Rothlisberger, U. Mixed Quantum Mechanical/Molecular Mechanical Molecular Dynamics Simulations of Biological Systems in Ground and Electronically Excited States. *Chem. Rev.* **115**, 6217-6263 (2015).
61. Grimme, S.; Waletzke, M. A Combination of Kohn-Sham Density Functional Theory and Multi-Reference Configuration Interaction Methods. *J. Chem. Phys.* **111**, 5645-5655 (1999).
62. Levine, B.G.; Ko, C.; Quenneville, J.; Martinez, T.J. Conical Intersections and Double Excitations in Time-Dependent Density Functional Theory. *Mol. Phys.* **104**, 1039-1051 (2006).
63. Šali, A.; Blundell, T.L. Comparative Protein Modelling by Satisfaction of Spatial Restraints. *J. Mol. Biol.* **234**, 779-815 (1993).
64. Nathans, J.; Hogness, D.S. Isolation and Nucleotide Sequence of the Gene Encoding Human Rhodopsin. *Proc. Natl. Acad. Sci. U. S. A.* **81**, 4851-4855 (1984).
65. *Expasy Molecular Biology Server* (see [www.expasy.org/genomics](http://www.expasy.org/genomics)).
66. *Human Gene Mutation Database* (see [www.hgmd.cf.ac.uk](http://www.hgmd.cf.ac.uk)).
67. Hubbard, R. Absorption Spectrum of Rhodopsin: 500 nm Absorption Band. *Nature* **221**, 432-435 (1969).
68. van Hazel, I.; Dungan, S.Z.; Hauser, F.E.; Morrow, J.M.; Endler, J.A.; Chang, B.S. A Comparative Study of Rhodopsin Function in the Great Bowerbird (*Ptilonorhynchus nuchalis*): Spectral Tuning and Light-Activated Kinetics. *Protein Sci.* **25**, 1308-1318 (2016).
69. Morrow, J.M.; Castiglione, G.M.; Dungan, S.Z.; Tang, P.L.; Bhattacharyya, N.; Hauser, F.E.; Chang, B.S. An Experimental Comparison of Human and Bovine Rhodopsin Provides Insight into the Molecular Basis of Retinal Disease. *FEBS Letters* **591**, 1720-1731 (2017).

70. Altschul, S.F.; Gish, W.; Miller, W.; Myers, E.W.; Lipman, D.J. Basic Local Alignment Search Tool. *J. Mol. Biol.* **215**, 403-410 (1990).
71. Altun, A.; Yokoyama, S.; Morokuma, K. Quantum Mechanical/Molecular Mechanical Studies on Spectral Tuning Mechanisms of Visual Pigments and Other Photoactive Proteins. *Photochem. Photobiol.* **84**, 845-854 (2008).
72. MacKerell, A.D., Jr.; Bashford, D.; Bellott, M.; Dunbrack, R.L.; Evanseck, J.D.; Field, M.J.; Fischer, S.; Gao, J.; Guo, H.; Ha, S.; Joseph-McCarthy, D.; Kuchnir, L.; Kuczera, K.; Lau, F.T.K.; Mattos, C.; Michnick, S.; Ngo, T.; Nguyen, D.T.; Prodhom, B.; Reiher, W.E., III; Roux, B.; Schlenkrich, M.; Smith, J.C.; Stote, R.; Straub, J.; Watanabe, M.; Wiorkiewicz-Kuczera, J.; Yin, D.; Karplus, M. All-Atom Empirical Potential for Molecular Modeling and Dynamics Studies of Proteins. *J. Phys. Chem. B* **102**, 3586-3616 (1998).
73. Chen, C.; Jiang, Y.; Koutalos, Y. Dynamic Behavior of Rod Photoreceptor Disks. *Biophys. J.* **83**, 1403-1412 (2002).
74. Li, H.; Robertson, A.D.; Jensen, J.H. Very Fast Empirical Prediction and Rationalization of Protein pK<sub>a</sub> Values. *Proteins: Struct., Funct., Bioinf.* **61**, 704-721 (2005).
75. Olsson, M.H.; Søndergaard, C.R.; Rostkowski, M.; Jensen, J.H. PROPKA3: Consistent Treatment of Internal and Surface Residues in Empirical pK<sub>a</sub> Predictions. *J. Chem. Theory Comput.* **7**, 525-537 (2011).
76. Søndergaard, C.R.; Olsson, M.H.M.; Rostkowski, M.; Jensen, J.H. Improved Treatment of Ligands and Coupling Effects in Empirical Calculation and Rationalization of pK<sub>a</sub> Values. *J. Chem. Theory Comput.* **7**, 2284-2295 (2011).
77. Mollevanger, L.C.P.J.; Kentgens, A.P.M.; Pardoën, J.A.; Courtin, J.M.L.; Veeman, W.S.; Lugtenburg, J.; De Grip, W.J. High-Resolution Solid-State <sup>13</sup>C-NMR Study of Carbons C-5 and C-12 of the Chromophore of Bovine Rhodopsin: Evidence for a 6-S-*cis* Conformation with Negative-Charge Perturbation near C-12. *Eur. J. Biochem.* **163**, 9-14 (1987).
78. Han, M.; Smith, S.O. NMR Constraints on the Location of the Retinal Chromophore in Rhodopsin and Bathorhodopsin. *Biochemistry* **34**, 1425-1432 (1995).
79. Birge, R.R.; Murray, L.P.; Pierce, B.M.; Akita, H.; Balogh-Nair, V.; Findsen, L.A.; Nakanishi, K. Two-Photon Spectroscopy of Locked-11-*cis*-Rhodopsin: Evidence for a Protonated Schiff Base in a Neutral Protein Binding Site. *Proc. Natl. Acad. Sci. U.S.A.* **82**, 4117-4121 (1985).
80. Sekharan, S.; Buss, V. Glutamic Acid 181 Is Uncharged in Dark-Adapted Visual Rhodopsin. *J. Am. Chem. Soc.* **130**, 17220-17221 (2008).
81. Röhrig, U.F.; Guidoni, L.; Rothlisberger, U. Early Steps of the Intramolecular Signal Transduction in Rhodopsin Explored by Molecular Dynamics Simulations. *Biochemistry* **41**, 10799-10809 (2002).
82. Frähmcke, J.S.; Wanko, M.; Phatak, P.; Mroginiski, M.A.; Elstner, M. The Protonation State of Glu181 in Rhodopsin Revisited: Interpretation of Experimental Data on the Basis of QM/MM Calculations. *J. Phys. Chem. B* **114**, 11338-11352 (2010).
83. Xiong, B.; Bellen, H.J. Rhodopsin Homeostasis and Retinal Degeneration: Lessons from the Fly. *Trends Neurosci.* **36**, 652-660 (2013).
84. Anderson, R.E.; Hollyfield, J.G.; LaVail, M.M. *Degenerative Diseases of the Retina*, (Springer Science & Business Media, 2012).
85. Zhukovsky, E.A.; Oprian, D.D. Effect of Carboxylic Acid Side Chains on the Absorption Maximum of Visual Pigments. *Science* **246**, 928-930 (1989).
86. Sakmar, T.P.; Franke, R.R.; Khorana, H.G. Glutamic Acid-113 Serves as the Retinylidene Schiff Base Counterion in Bovine Rhodopsin. *Proc. Natl. Acad. Sci. U. S. A.* **86**, 8309-8313 (1989).
87. Zhang, T.; Cao, L.-H.; Kumar, S.; Enemchukwu, N.O.; Zhang, N.; Lambert, A.; Zhao, X.; Jones, A.; Wang, S.; Dennis, E.M. Dimerization of Visual Pigments *in Vivo*. *Proc. Natl. Acad. Sci. U S A* **113**, 9093-9098 (2016).
88. Sikora, S.; Little, A.S.; Dewey, T.G. Room Temperature Trapping of Rhodopsin Photointermediates. *Biochemistry* **33**, 4454-4459 (1994).

89. Xie, P.; Zhou, P.; Alsaedi, A.; Zhang, Y. pH-Dependent Absorption Spectra of Rhodopsin Mutant E113Q: On the Role of Counterions and Protein. *Spectrochim. Acta, Part A* **174**, 25-31 (2017).
90. Valsson, O.; Campomanes, P.; Tavernelli, I.; Rothlisberger, U.; Filippi, C. Rhodopsin Absorption from First Principles: Bypassing Common Pitfalls. *J. Chem. Theory Comput.* **9**, 2441-2454 (2013).
91. Feldman, T.; Ostrovsky, M.; Kholmurodov, K.; Yasuoka, K. Model of Abnormal Chromophore-Protein Interaction for E181K Rhodopsin Mutation: Computer Molecular Dynamics Study. *Open Biochem. J.* **6**, 94-102 (2012).
92. Wald, G.; Brown, P.K. Human Rhodopsin. *Science* **127**, 222-249 (1958).
93. Andruniów, T.; Olivucci, M. How Does the Relocation of Internal Water Affect Resonance Raman Spectra of Rhodopsin? An Insight from CASSCF/Amber Calculations. *J. Chem. Theory Comput.* **5**, 3096-3104 (2009).
94. Fujimoto, K.; Hayashi, S.; Hasegawa, J.-Y.; Nakatsuji, H. Theoretical Studies on the Color-Tuning Mechanism in Retinal Proteins. *J. Chem. Theory Comput.* **3**, 605-618 (2007).
95. Jorgensen, W.L.; Chandrasekhar, J.; Madura, J.D.; Impey, R.W.; Klein, M.L. Comparison of Simple Potential Functions for Simulating Liquid Water. *J. Chem. Phys.* **79**, 926-928 (1983).
96. Phillips, J.C.; Braun, R.; Wang, W.; Gumbart, J.; Tajkhorshid, E.; Villa, E.; Chipot, C.; Skeel, R.D.; Kale, L.; Schulten, K. Scalable Molecular Dynamics with NAMD. *J. Comput. Chem.* **26**, 1781-1802 (2005).
97. MacKerell, A.D., Jr.; Feig, M.; Brooks, C.L., III. Extending the Treatment of Backbone Energetics in Protein Force Fields: Limitations of Gas-Phase Quantum Mechanics in Reproducing Protein Conformational Distributions in Molecular Dynamics Simulations. *J. Comput. Chem.* **25**, 1400-1415 (2004).
98. Essmann, U.; Perera, L.; Berkowitz, M.L.; Darden, T.; Lee, H.; Pedersen, L.G. A Smooth Particle Mesh Ewald Method. *J. Chem. Phys.* **103**, 8577-8593 (1995).
99. Ryckaert, J.-P.; Ciccotti, G.; Berendsen, H.J. Numerical Integration of the Cartesian Equations of Motion of a System with Constraints: Molecular Dynamics of N-Alkanes. *J. Comput. Phys.* **23**, 327-341 (1977).
100. Nosé, S. A Unified Formulation of the Constant Temperature Molecular Dynamics Methods. *J. Chem. Phys.* **81**, 511-519 (1984).
101. Humphrey, W.; Dalke, A.; Schulten, K. VMD - Visual Molecular Dynamics. *J. Mol. Graphics* **14**, 33-38 (1996).
102. *ChemShell, a Computational Chemistry Shell* (see [www.chemshell.org](http://www.chemshell.org)).
103. Metz, S.; Kästner, J.; Sokol, A.A.; Keal, T.W.; Sherwood, P. Chemshell—a Modular Software Package for QM/MM Simulations. *Wiley Interdiscip. Rev. Comput. Mol. Sci.* **4**, 101-110 (2014).
104. Sherwood, P.; de Vries, A.H.; Guest, M.F.; Schreckenbach, G.; Catlow, C.R.A.; French, S.A.; Sokol, A.A.; Bromley, S.T.; Thiel, W.; Turner, A.J.; Billeter, S.; Terstegen, F.; Thiel, S.; Kendrick, J.; Rogers, S.C.; Casci, J.; Watson, M.; King, F.; Karlsen, E.; Sjøvoll, M.; Fahmi, A.; Schafer, A.; Lennartz, C. Quasi: A General Purpose Implementation of the QM/MM Approach and Its Application to Problems in Catalysis. *THEOCHEM* **632**, 1-28 (2003).
105. Frisch, M.J. *et al.* Gaussian 09, Revision A.02; Gaussian, Inc.: Wallingford, CT. (2009).
106. Smith, W.; Forester, T.R. DL\_POLY\_2.0: A General-Purpose Parallel Molecular Dynamics Simulation Package. *J. Mol. Graphics* **14**, 136-141 (1996).
107. Vosko, S.H.; Wilk, L.; Nusair, M. Accurate Spin-Dependent Electron Liquid Correlation Energies for Local Spin Density Calculations: A Critical Analysis. *Can. J. Phys.* **58** 1200-1211 (1980).
108. Becke, A.D. Density-Functional Exchange-Energy Approximation with Correct Asymptotic Behavior. *Phys. Rev. A* **38**, 3098-3100 (1988).
109. Becke, A.D. Density-Functional Thermochemistry. III. The Role of Exact Exchange. *J. Chem. Phys.* **98**, 5648-5652 (1993).
110. Slater, J.C. A Simplification of the Hartree-Fock Method. *Phys. Rev. A* **81**, 385-390 (1951).
111. Schäfer, A.; Huber, C.; Ahlrichs, R. Fully Optimized Contracted Gaussian Basis Sets of Triple Zeta Valence Quality for Atoms Li to Kr. *J. Chem. Phys.* **100** 5829-5835 (1994).

112. Melaccio, F.; del Carmen Marín, M.; Valentini, A.; Montisci, F.; Rinaldi, S.; Cherubini, M.; Yang, X.; Kato, Y.; Stenrup, M.; Orozco-Gonzalez, Y. Toward Automatic Rhodopsin Modeling as a Tool for High-Throughput Computational Photobiology. *J. Chem. Theory Comput.* **12**, 6020-6034 (2016).
113. Altun, A.; Yokoyama, S.; Morokuma, K. Mechanism of Spectral Tuning Going from Retinal *in Vacuo* to Bovine Rhodopsin and Its Mutants: Multireference *Ab Initio* Quantum Mechanics/Molecular Mechanics Studies. *J. Phys. Chem. B* **112**, 16883-16890 (2008).
114. González-Luque, R.; Olaso-González, G.; Merchán, M.; Coto, P.B.; Serrano-Andrés, L.; Garavelli, M. On the Role of the Triplet State in the *cis/trans* Isomerization of Rhodopsin: A CASPT2//CASSCF Study of a Model Chromophore. *Int. J. Quantum Chem.* **111**, 3431-3437 (2011).
115. Kästner, J.; Carr, J.M.; Keal, T.W.; Thiel, W.; Wander, A.; Sherwood, P. DL-Find: An Open-Source Geometry Optimizer for Atomistic Simulations. *J. Phys. Chem. A* **113** 11856–11865 (2009).
116. Bakowies, D.; Thiel, W. Hybrid Models for Combined Quantum Mechanical and Molecular Mechanical Approaches. *J. Phys. Chem.* **100**, 10580-10594 (1996).
117. de Vries, A.H.; Sherwood, P.; Collins, S.J.; Rigby, A.M.; Rigutto, M.; Kramer, G.J. Zeolite Structure and Reactivity by Combined Quantum-Chemical–Classical Calculations. *J. Phys. Chem. B* **103**, 6133–6141 (1999).
118. Sherwood, P.; deVries, A.H.; Collins, S.J.; Greatbanks, S.P.; Burton, N.A.; Vincent, M.A.; Hillier, I.H. Computer Simulation of Zeolite Structure and Reactivity Using Embedded Cluster Methods. *Faraday Discuss* **106** 79–92 (1997).
119. Koopmans, T. Über Die Zuordnung Von Wellenfunktionen Und Eigenwerten Zu Den Einzelnen Elektronen Eines Atoms. *Physica* **1**, 104-113 (1934).
120. Sen, K.; Thiel, W. Role of Two Alternate Water Networks in Compound I Formation in P450eryF. *J. Phys. Chem. B* **118** 2810–2820 (2014).
121. Polyak, I.; Reetz, M.T.; Thiel, W. Quantum Mechanical/Molecular Mechanical Study on the Mechanism of the Enzymatic Baeyer–Villiger Reaction. *J. Am. Chem. Soc.* **134** 2732–2741 (2012).
122. Karasulu, B.; Patil, M.; Thiel, W. Amine Oxidation Mediated by Lysine-Specific Demethylase 1: Quantum Mechanics/Molecular Mechanics Insights into Mechanism and Role of Lysine 661. *J. Am. Chem. Soc.* **135**, 13400–13413 (2013).
123. Escorcia, A.M.; Stein, M. QM/MM Investigation of the Role of a Second Coordination Shell Arginine in [NiFe]-Hydrogenases. *Front. Chem.* **6** (2018).
124. Bustamante, J.P.; Radusky, L.; Boechi, L.; Estrin, D.A.; ten Have, A.; Martí, M.A. Evolutionary and Functional Relationships in the Truncated Hemoglobin Family. *PLoS Comput. Biol.* **12**, e1004701 (2016).
125. Chovancova, E.; Pavelka, A.; Benes, P.; Strnad, O.; Brezovsky, J.; Kozlikova, B.; Gora, A.; Sustr, V.; Klvana, M.; Medek, P. Caver 3.0: A Tool for the Analysis of Transport Pathways in Dynamic Protein Structures. *PLoS Comput. Biol.* **8**, e1002708 (2012).
126. Kozlikova, B.; Sebestova, E.; Sustr, V.; Brezovsky, J.; Strnad, O.; Daniel, L.; Bednar, D.; Pavelka, A.; Manak, M.; Bezdeka, M. Caver Analyst 1.0: Graphic Tool for Interactive Visualization and Analysis of Tunnels and Channels in Protein Structures. *Bioinformatics* **30**, 2684-2685 (2014).
127. Padrón, J.A.G.; Crespo, R.O.; Hernández-Rodríguez, E.W.; Garriga, P.; Montero, L.A.; García-Piñeiro, J.C. Patterns of Retinal Light Absorption Related to Retinitis Pigmentosa Mutants from *in Silico* Model Structures of Rhodopsin. *Proteins: Struct. Funct. Bioinf.* **57**, 392-399 (2004).
128. Valley, C.C.; Cembran, A.; Perlmutter, J.D.; Lewis, A.K.; Labello, N.P.; Gao, J.; Sachs, J.N. The Methionine-Aromatic Motif Plays a Unique Role in Stabilizing Protein Structure. *J. Biol. Chem.* **287**, 34979-34991 (2012).
129. Scharlin, P.; Battino, R.; Silla, E.; Tunon, I.; Pascual-Ahuir, J. Solubility of Gases in Water: Correlation between Solubility and the Number of Water Molecules in the First Solvation Shell. *Pure Appl. Chem.* **70**, 1895-1904 (1998).
130. Hasegawa, J.-Y.; Fujimoto, K.J.; Nakatsuji, H. Color Tuning in Photofunctional Proteins. *ChemPhysChem* **12**, 3106-3115 (2011).

131. Demoulin, B.; El-Tahawy, M.M.; Nenov, A.; Garavelli, M.; Le Bahers, T. Intramolecular Photo-Induced Charge Transfer in Visual Retinal Chromophore Mimics: Electron Density-Based Indices at the TD-DFT and Post-HF Levels. *Theor. Chem. Acc.* **135**, 96 (2016).
132. Pirillo, J.; Mazzone, G.; Russo, N.; Bertini, L. Photophysical Properties of S, Se and Te-Substituted Deoxyguanosines: Insight into Their Ability to Act as Chemotherapeutic Agents. *J. Chem. Inf. Mod.* **57**, 234-242 (2017).
133. Ala-Laurila, P.; Donner, K.; Koskelainen, A. Thermal Activation and Photoactivation of Visual Pigments. *Biophys. J.* **86**, 3653-3662 (2004).
134. Sekharan, S.; Morokuma, K. QM/MM Study of the Structure, Energy Storage, and Origin of the Bathochromic Shift in Vertebrate and Invertebrate Bathorhodopsins. *J. Am. Chem. Soc.* **133**, 4734-4737 (2011).
135. Gascon, J.A.; Batista, V.S. QM/MM Study of Energy Storage and Molecular Rearrangements Due to the Primary Event in Vision. *Biophys. J.* **87**, 2931-2941 (2004).
136. Kim, J.E.; Tauber, M.J.; Mathies, R.A. Wavelength Dependent *cis-trans* Isomerization in Vision. *Biochemistry* **40**, 13774-13778 (2001).
137. Washington, I.; Brooks, C.; Turro, N.J.; Nakanishi, K. Porphyrins as Photosensitizers to Enhance Night Vision. *J. Am. Chem. Soc.* **126**, 9892-9893 (2004).
138. Fisher, M.M.; Weiss, K. Laser Photolysis of Retinal and Its Protonated and Unprotonated N-Butylamine Schiff Base. *Photochem. Photobiol.* **20**, 423-432 (1974).
139. Salice, P.; Arnbjerg, J.; Pedersen, B.W.; Toftegaard, R.; Beverina, L.; Pagani, G.A.; Ogilby, P.R. Photophysics of Squaraine Dyes: Role of Charge-Transfer in Singlet Oxygen Production and Removal. *J. Phys. Chem. A* **114**, 2518-2525 (2010).
140. Edge, R.; Truscott, T.G. Singlet Oxygen and Free Radical Reactions of Retinoids and Carotenoids—A Review. *Antioxidants* **7**, 5 (2018).
141. DeRosa, M.C.; Crutchley, R.J. Photosensitized Singlet Oxygen and Its Applications. *Coord. Chem. Rev.* **233-234**, 351-371 (2002).
142. Sekharan, S.; Sugihara, M.; Buss, V. Origin of Spectral Tuning in Rhodopsin—It Is Not the Binding Pocket. *Angew. Chem., Int. Ed.* **46**, 269-271 (2007).
143. Liu, Y.; Wu, H.; Li, M.; Yin, J.-J.; Nie, Z. pH Dependent Catalytic Activities of Platinum Nanoparticles with Respect to the Decomposition of Hydrogen Peroxide and Scavenging of Superoxide and Singlet Oxygen. *Nanoscale* **6**, 11904-11910 (2014).
144. Herrera-Hernández, M.G.; Ramon, E.; Lupala, C.S.; Tena-Campos, M.; Pérez, J.J.; Garriga, P. Flavonoid Allosteric Modulation of Mutated Visual Rhodopsin Associated with Retinitis Pigmentosa. *Sci. Rep.* **7**, 1-13 (2017).

## For Table of Contents Use Only

### ***Multi-scale Simulation Reveals that an Amino Acid Substitution Increases Photosensitizing Reaction Inputs in Rhodopsins***

*Erix W. Hernández-Rodríguez\**, *Andrés M. Escorcía*, *Marc W. van der Kamp*, *Ana L. Montero-Alejo*, and *Julio Caballero*.

